

Volatile Organic Compound Detection Using Insect Odorant-Receptor Functionalised Field-Effect Transistors

by

Eddyn Oswald Perkins Treacher

A thesis submitted in fulfilment of the
requirements of the degree of
Doctor of Philosophy in Physics
School of Physical and Chemical Sciences
Te Herenga Waka - Victoria University of Wellington

Nov 2023



Table of contents

Acknowledgements	1
1. Characteristics of Pristine Carbon Nanotube & Graphene Field Effect Transistors	3
1.1. Introduction	3
1.2. Carbon Nanotube Network Morphology	4
1.2.1. Atomic Force Microscopy	4
1.2.2. Raman Spectroscopy	10
1.3. Electrical Characteristics of Pristine Devices	12
1.3.1. Carbon Nanotube Network Devices	12
1.3.2. Graphene Devices	16
1.4. Real-Time Salt Concentration Sensing with Phosphate Buffered Saline . .	19
1.4.1. Control Series and Baseline Drift	19
1.4.2. Sensing Series	23
1.5. Conclusion	27
Appendices	29
A. Python Code for Data Analysis	29
A.1. Code Repository	29
A.2. Atomic Force Microscope Histogram Analysis	29
A.3. Raman Spectroscopy Analysis	29
A.4. Field-Effect Transistor Analysis	29

Acknowledgements

69450

Rifat, Alex - vapour sensor
Erica Cassie - FET sensing setup
Rob Keyzers and Jennie Ramirez-Garcia - NMR spectra
Patricia Hunt - Computational chemistry

1. Characteristics of Pristine Carbon Nanotube & Graphene Field Effect Transistors

280656

1.1. Introduction

A range of methods were followed to fabricate carbon nanotube network and graphene field-effect transistors for biosensor use. This chapter therefore looks to use the characterisation techniques outlined in the previous chapter to compare and contrast the device channel morphologies and electrical characteristics resulting from various methods.

The three carbon nanotube film types used for devices were the solvent-deposited, surfactant-deposited and steam-assisted surfactant-deposited (steam-deposited) films discussed in the previous chapter. Atomic force microscopy and Raman spectroscopy was performed on the carbon nanotube networks to identify the distribution of carbon nanotube diameters and the defects present on the carbon nanotube networks. Electrical characterisation was then used to see how the morphology of each film type affects the performance of the completed devices. Both back-gated and liquid-gated transfer characteristics were compared, as well as key parameters taken from the liquid-gated characteristics. The electrical behaviour of liquid-gated graphene devices was also examined, as well as the impact of water on the performance of back-gated devices for vapour sensing use.

Finally, as a control measurement for liquid-gated sensing and to verify the behaviour of the pristine device as a sensor, a salt concentration sensing series was performed with a steam-deposited carbon nanotube network device. The device characteristics were taken and device drift was examined and modelled. The sensing series was performed by successively diluting 1XPBS electrolyte in the polydimethylsiloxane ‘well’ (electrolyte container) while passing a current through the device, and measuring the current response to dilutions. Various filters were applied to the collected data to better understand the signal change.

1.2. Carbon Nanotube Network Morphology

1.2.1. Atomic Force Microscopy

Figure 1.1 shows a side-by-side comparison of the surface morphology of carbon nanotube films fabricated using the methods described in [?@sec-dep-carbon-nanotubes](#). These images were collected using an atomic force microscope and processed in the manner described in [?@sec-afm-characterisation](#). Figure 1.1a shows a film of carbon nanotubes deposited in solvent, Figure 1.1c shows a film of carbon nanotubes dropcast in surfactant, and Figure 1.1e shows carbon nanotubes dropcast in surfactant in the presence of steam. As discussed in previous works using solvent-based deposition techniques for depositing carbon nanotubes, in each network multi-tube bundles form due to strong mutual attraction between nanotubes [1]–[4]. However, when surfactants are present, they adsorb onto the carbon nanotubes and form a highly repulsive structure able to overcome the strong attraction between nanotubes. This repulsion keeps the individual carbon nanotubes more isolated [5]–[9]. The diameter range provided by the supplier for the individual carbon nanotubes used is 1.2 – 1.7 nm, while the length range is 0.3 – 5.0 μm (Nanointegris).

It has previously been demonstrated that the diameter range of deposited single-walled carbon nanotubes can be modelled via a normal or Gaussian distribution [10]–[12]. However, when we directly extract and bin the height profiles from the $2.5 \mu\text{m} \times 2.5 \mu\text{m}$ AFM images, plotted in black in Figure 1.1, we obtain histograms which do not follow a normal distribution. One reason for this result is the surface roughness of the silicon dioxide substrate. The carbon nanotubes do not lie perfectly level on a perfectly level silicon oxide substrate. In practice, both the SiO_2 substrate and the surface of the carbon nanotubes both have a degree of roughness. To find the contribution of surface roughness to the height profile histogram corresponding to each network deposition method, silicon dioxide substrates were modified using the same processes as in Figure 1.1 but without carbon nanotubes present in the solutions used. $2.5 \mu\text{m} \times 2.5 \mu\text{m}$ AFM images of the modified surfaces are shown in Figure 1.2.

In Figure 1.2, we see that each substrate surface has a roughness that follows a normal distribution with some degree of skewness. Figure 1.2b and Figure 1.2d are negatively skewed distributions. The fitted skew-normal distribution in Figure 1.2b has a skew parameter α (or shape parameter) of -3.2, a location parameter ξ of 2.2 nm and a scale parameter ω of 0.5 nm, while in Figure 1.2d $\alpha = -2.2$, $\xi = 2.2$ nm and $\omega = 0.5$ nm. ξ and ω correspond to the mean and standard deviation of the skew-free normal distribution when α is set equal to zero [13]. The close correspondence between ξ and ω for these distributions but not α implies that the skewness is a variable imaging or processing artifact rather than a physical property of the surface. Without distortion, the roughness of a clean SiO_2 surface should follow a normal distribution [14].

However, Figure 1.2f has a pronounced positive skew with a long tail. The tail appears to result from the contribution of residual surfactant to surface morphology, observed

1.2. Carbon Nanotube Network Morphology

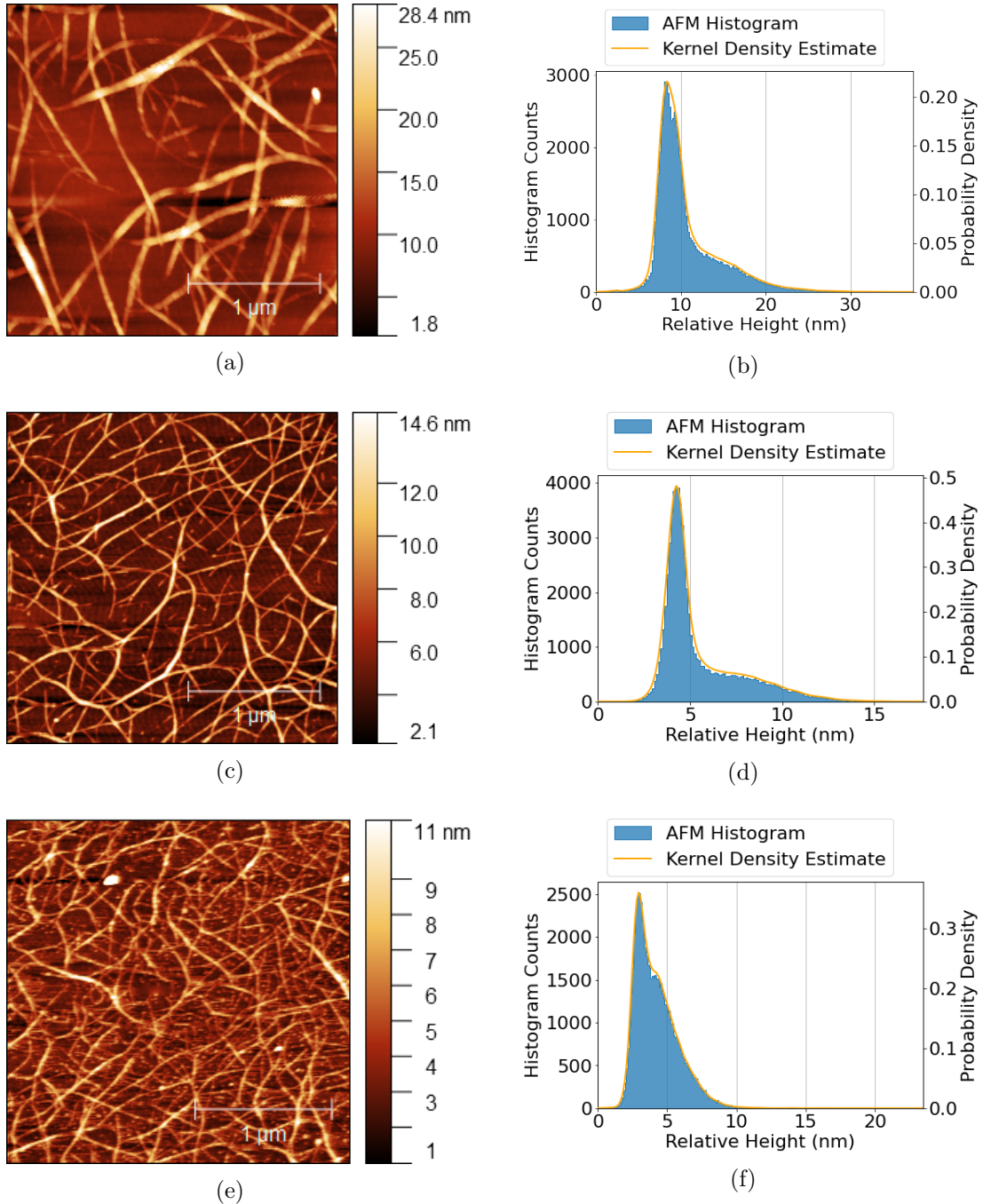


Figure 1.1.: $2.5 \mu\text{m} \times 2.5 \mu\text{m}$ atomic force microscope (AFM) images of carbon nanotube films deposited using various methods, shown side-by-side with histogram height distributions and kernel density estimate (KDE) plots corresponding to each image. The network shown in (a) with height distribution shown in (b) was deposited in solvent, the network shown in (c) with height distribution shown in (d) was dropcast in surfactant, and the network shown in (e) with height distribution shown in (f) was dropcast in surfactant with steam present.

1. Characteristics of Pristine Carbon Nanotube & Graphene Field Effect Transistors

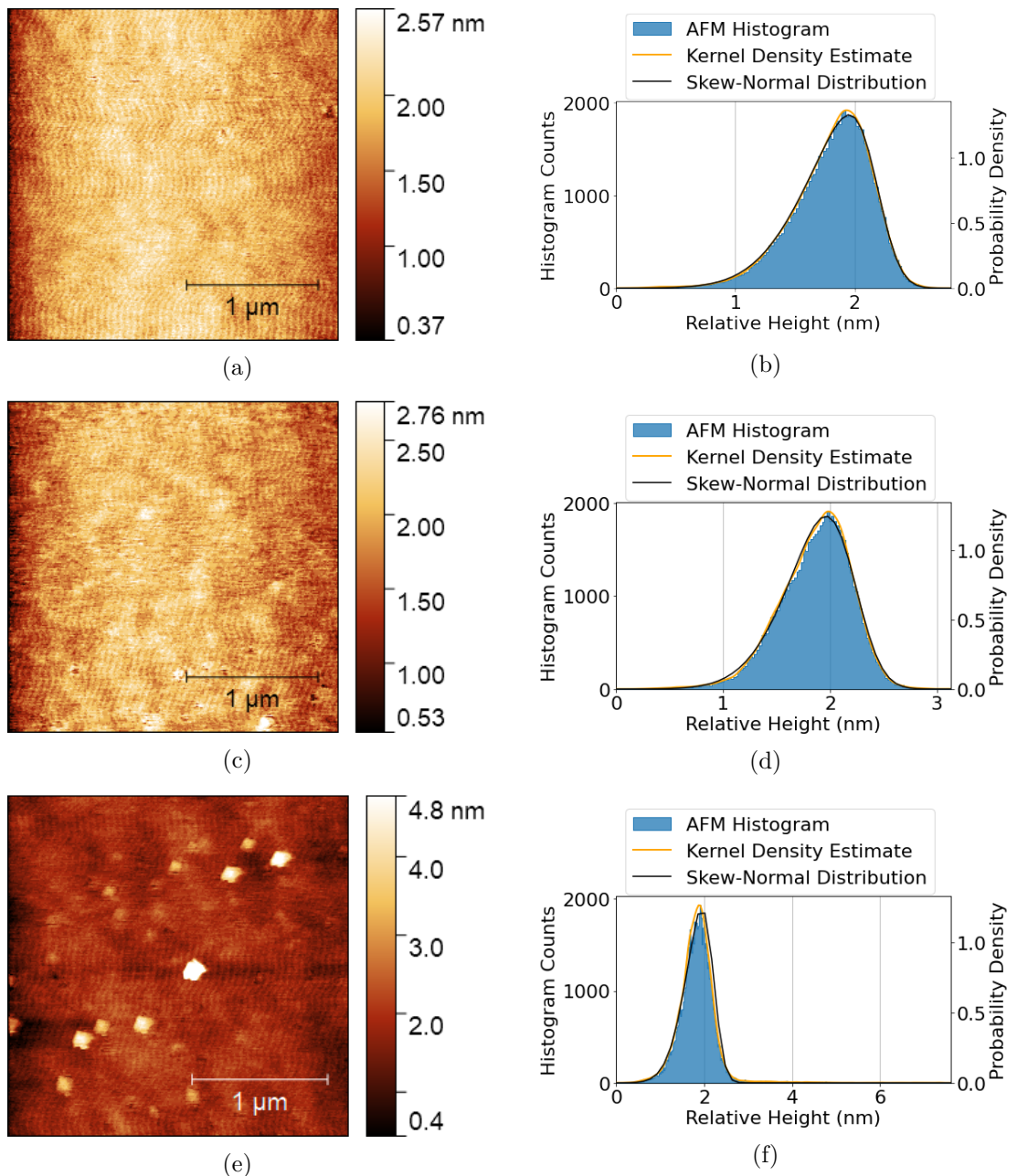


Figure 1.2.: $2.5 \mu\text{m} \times 2.5 \mu\text{m}$ atomic force microscope (AFM) images of silicon dioxide substrates alongside histogram height distributions and KDE plots corresponding to each image. The substrate in (a) and (b) was exposed to solvent, the substrate in (c) and (d) was exposed to surfactant, and the substrate in (e) and (f) was exposed to surfactant with steam present.

1.2. Carbon Nanotube Network Morphology

in Figure 1.2e and discussed elsewhere in the literature [12]. Attempting to fit a skew-normal distribution to this histogram fails when all three variables are allowed to vary due to the presence of the tail. Instead, we fix ξ and ω at 2.2 nm and 0.5 nm respectively to mimic the silicon dioxide distributions previously obtained, and only α is allowed to vary during the fitting process. The result is shown in Figure 1.2f. The fitted distribution has an α of -2.4. The distribution closely fits the negative tail of the histogram, but deviates slightly from the positive tail due to the presence of surfactant. Since this deviation is small, the quality of the fit is still reasonably high, with an R-squared value of 0.98. Surfactant contamination could have negative effects on both sensitivity of carbon nanotubes and also could damage attached biological elements.

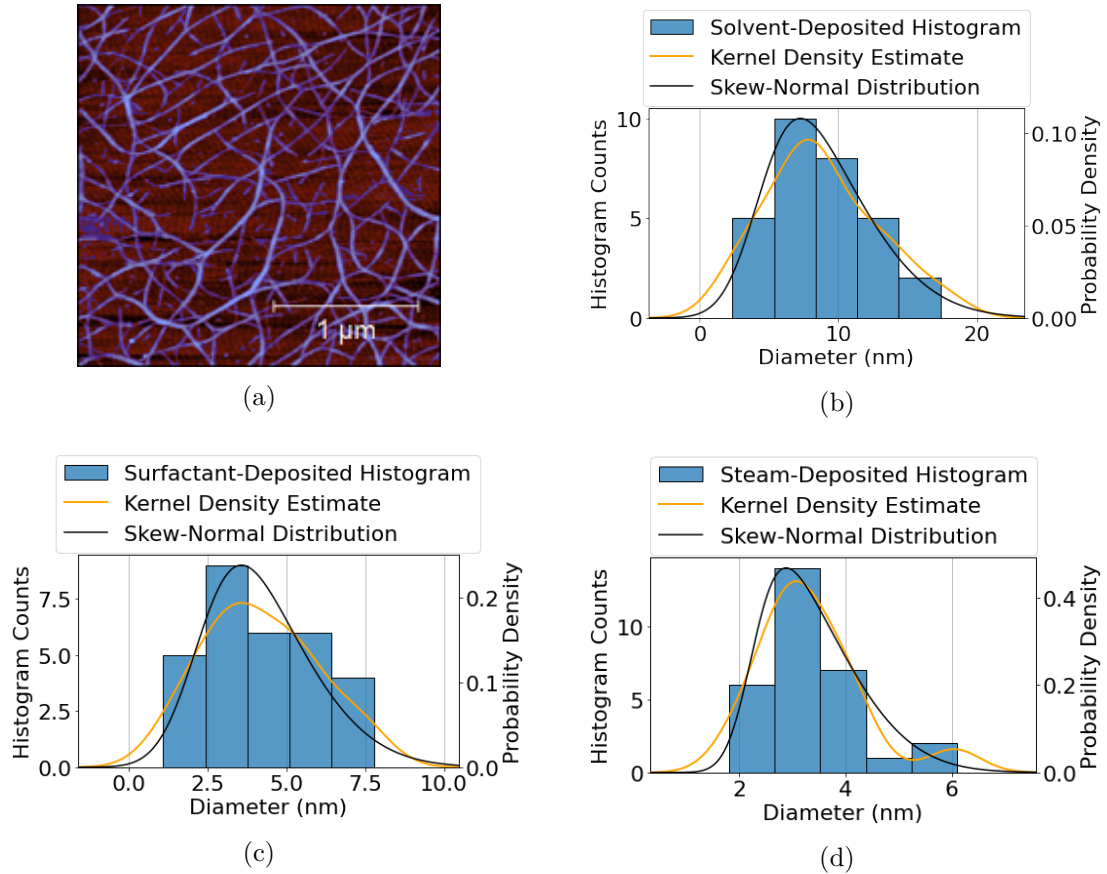


Figure 1.3.: An masked AFM image is shown in (a), where the masked carbon nanotube bundles are shaded blue. The mask sets a height threshold so that masked features are excluded from the height dataset. Histogram height distributions with corresponding KDE plots collected via the morphology analysis method outlined by Vobornik *et al.* [12] are shown in (b)-(d). The substrate in (b) was exposed to solvent, the substrate in (c) was exposed to surfactant, and the substrate in (d) was exposed to surfactant with steam present.

1. Characteristics of Pristine Carbon Nanotube & Graphene Field Effect Transistors

Using the morphology analysis technique outlined by Vobornik *et al.* [12], we collected five successive diameter measurements of 30 carbon nanotube bundles using Gwyddion. Measurements were not taken at bundle junctions. A height threshold ‘mask’ was defined in Gwyddion to determine average substrate height, as shown in Figure 1.3a. This background value was subtracted from our diameter measurements to determine the actual bundle height. The means of the solvent-deposited, surfactant-deposited and steam-assisted surfactant-deposited bundle diameter histograms are 8.8 ± 4.0 nm, 4.2 ± 1.8 nm and 3.3 ± 1.0 nm respectively. We see that an increased maximum feature height leads to an increased mean background height, and by examining the AFM images in Figure 1.1 we see that this may be due to deep artifacts on the surface of the substrate in the vicinity of large features. The average of the five height-adjusted values for each carbon nanotube bundle was then calculated, and these 30 averages were sorted into six equal-sized bins. The binned bundle diameter measurements, alongside estimated probability density, are shown in Figure 1.3.

We notice from Figure 1.3 that each histogram appears to follow a positively skewed normal distribution, different to the skew-free normal distribution we expect from previous works [10]–[12]. The skew is likely another artifact from imaging the network with the atomic force microscope. The force of the atomic force microscope tip is known to cause larger bundles to undergo some degree of compression, and the resulting systematic underestimation of their height may be responsible for the distribution skewness [12]. The fitted skew-normal distribution in Figure 1.3b has $\alpha = 2.7$, $\xi = 4.3$ nm, $\omega = 5.9$ nm, the distribution in Figure 1.3c has $\alpha = 2.4$, $\xi = 2.2$ nm, $\omega = 2.6$ nm, and the distribution in Figure 1.3d has $\alpha = 3.6$, $\xi = 2.2$ nm and $\omega = 1.5$ nm. We notice that the probability density for the carbon nanotube bundle histogram drops to approximately zero at or before 0 nm, as is physically appropriate.

Table 1.1.: The first eight optimised ratios of 2D packed circle diameter to encompassing circle diameter, given to 3 s.f. (encompassing circle diameter = d , number of packed circles = n , approximate packed circle diameter = d_n).

n	2	3	4	5	6	7	8	9
d/d_n	2.00	2.15	2.41	2.70	3.00	3.00	3.30	3.61

If we model carbon nanotube bundles as cylinders, and we assume the component nanotubes follow 2D packing and are of equal diameter, we can state the mean bundle size for each deposition type in terms of number of nanotubes n [2], [15], [16]. Table 1.1 shows the relationship between the diameter of a bundle and the constituent diameters of up to nine 2D packed carbon nanotubes within that bundle. Assuming an average carbon nanotube diameter of 1.45 nm, we can use the d/d_n packing ratios to obtain an estimate of the number of nanotubes in the mean bundle size for each deposition [16]. These estimates are shown in Table 1.2. Also shown in Table 1.2 is an estimate of the ratio of single- to multi-tube bundles for each deposition. This estimate was obtained

1.2. Carbon Nanotube Network Morphology

Table 1.2.: The mean of histogram distributions for carbon nanotube films deposited using various methods, alongside estimates for the number of nanotubes present per mean bundle and the estimated proportion of multi-tubed bundles present across the network.

	Mean Bundle Diameter (nm)	Tubes per Average Bundle	% Multi-Tube Bundles
Solvent deposited	8.8 ± 4.0	28	> 96%
Surfactant deposited	4.2 ± 1.8	5	> 75%
Surfactant deposited with steam	3.3 ± 1.0	3	> 65%

by taking the integral of each distribution with a lower bound of 2.9 nm, the minimum multi-tube bundle size for 1.45 nm diameter nanotubes. As the area under the curve represents the probability a bundle will have a particular diameter, this integral should give a good estimate of the relative proportion of multi-tube bundles. Table 1.2 should be interpreted as lower-limit estimates of the size and relative proportion of bundles, recalling that the distribution skewness indicates underestimation of the true bundle height.

Both the carbon nanotube bundle diameter mean and standard deviation are small for surfactant-deposited films when compared to the mean and standard deviation of solvent-deposited films. However, despite the presence of surfactant, it is apparent both from Figure 1.1 and Table 1.2 that not all surfactant-dispersed carbon nanotubes are deposited individually. Bundling may occur during the process of deposition onto the substrate, which could disrupt the repulsive forces from the surfactant coating and allow attractive forces to temporarily dominate. It is possible that the bundling of surfactant-dispersed carbon nanotubes is a consequence of dynamics introduced by the coffee-ring effect [17], [18]. The coffee-ring effect refers to a build-up of dispersed solid forming around the edges of a dispersion evaporating on a surface. This process occurs due to the dispersion edges being fixed by surface forces, leading to capillary flow outwards to replace liquid evaporating at the edges, bringing solid material along with it. The presence of vapour is known to disrupt this capillary effect [19], which may explain why mean bundle diameter is lower for the films deposited in surfactant with steam present relative to films deposited in surfactant without steam.

From this discussion, we can conclude that the histograms shown in Figure 1.1 are linear combinations of skewed normal distributions corresponding to both the substrate surface, with a negative skew, and the carbon nanotube bundles, with a positive skew. X and Y junctions between overlapping nanotubes may also form a similarly skewed normal distribution as part of the full histogram [2]. The complete linear combination could be modelled mathematically in order to rapidly extract key parameters from atomic force microscope images [20], but implementing this approach is outside of the scope of

1. Characteristics of Pristine Carbon Nanotube & Graphene Field Effect Transistors

this thesis. The prevalence of carbon nanotube bundling on the surface is lowered by the presence of surfactant during deposition. Introducing steam when depositing with surfactant lowers bundling even further, but also leads to residual surfactant pooling and attaching to the substrate surface. These results may both be explained by the presence of steam enabling surfactant to follow carbon nanotubes to the substrate surface, which keeps them from bundling during the attachment process. The unwanted persistence of surfactant means that higher temperature vacuum annealing may be required for robust biosensors [21].

1.2.2. Raman Spectroscopy

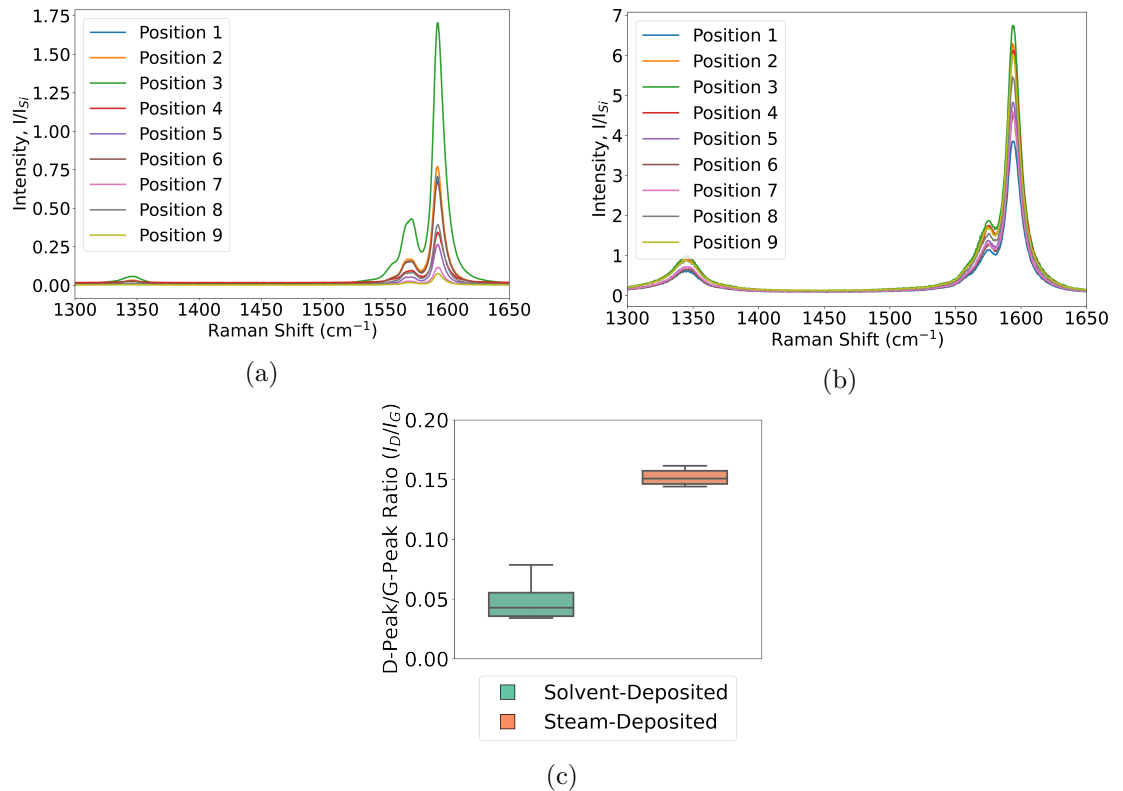


Figure 1.4.: A series of nine Raman spectra at different locations across a $10 \mu\text{m} \times 50 \mu\text{m}$ carbon nanotube film region, spaced at least $10 \mu\text{m}$ apart, with (a) showing spectra from a film deposited in solvent and (b) showing spectra from a film deposited in surfactant with steam present. (c) shows the spread of the D-peak/G-peak spectral ratios corresponding to each film.

Raman spectra were collected from a solvent-deposited carbon nanotube film and a steam-assisted surfactant-deposited film, both on silicon dioxide, in the manner described in ?@sec-raman-characterisation. These spectra were then processed us-

1.3. Electrical Characteristics of Pristine Devices

ing the Python script mentioned in Section A.3. For each location, spectra over two wavenumber ranges were collected. The silicon peak, found in the first range between 100 cm^{-1} and 210 cm^{-1} , was used to normalise the second spectrum between 1250 cm^{-1} and 1735 cm^{-1} . The silicon-peak normalised spectra are shown in Figure 1.4.

and the baseline region between 1400 and 1500 cm^{-1} is set as zero amplitude for data collected from each film location. The data from each location is then normalised to the D-peak (the maximum point on the D-peak, which lies between 1300 and 1400 cm^{-1} , is set equal to unity). Using these datasets, plots of normalised intensity relative to the D-peak comparing each location can be created. The ratio I^D/I_G can be found by taking the inverse of the maximum point on the G-peak of these normalised plots. A plot of the average intensity across all locations measured can also be created.

1.3. Electrical Characteristics of Pristine Devices

1.3.1. Carbon Nanotube Network Devices

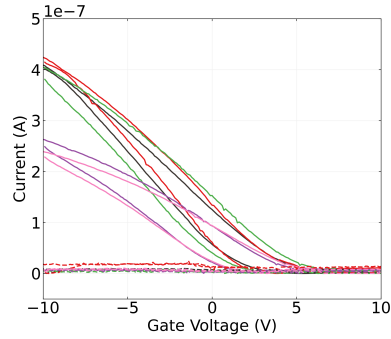
Each carbon nanotube device fabricated was electrically characterised as described in ?@sec-electrical-characterisation, and electrical data was analysed using the Python code discussed in Section A.4.

Figure 1.5 displays multi-channel measurements of representative devices fabricated as described in ?@sec-fabrication. To ensure a consistent comparison, each device here was encapsulated with AZ® 1518 encapsulation before measurements were taken. The channels which did not exhibit reliable transistor characteristics are not shown. These ‘non-working’ channels were either shorted, due to metal remaining on the channel after lift-off, or were very low current, due to a very sparse carbon nanotube network. Devices shown here with a solvent-deposited carbon nanotube network were fabricated prior to Jan 2022; devices with a surfactant-deposited network without steam present were fabricated prior to Jun 2021; devices with a surfactant-deposited network without steam were fabricated prior to Sep 2022.

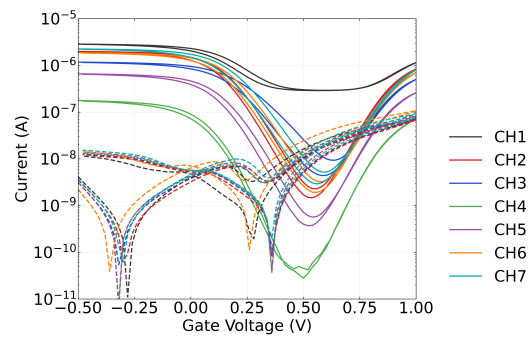
When backgated, devices exhibited *p*-type transistor behaviour with significant hysteresis and negligible gate current leakage. The presence of hysteresis can be explained by the presence of defects or charge traps within and on the surface of the silicon dioxide and at interfaces between the silicon dioxide and carbon nanotubes [22]–[24]. The devices fabricated with a solvent-based deposition were switched off at a lower voltage than the devices which used surfactant during deposition.

When the devices were liquid-gated with 1XPBS electrolyte, they exhibited ambipolar characteristics, commonly observed in carbon nanotube network FETs [2], [25]–[29]. When devices were appropriately configured, leakage current did not exceed $\sim 1 \times 10^{-7}\text{ V}$ across the forward and reverse sweep. Devices generally exhibited significantly less hysteresis than in the backgated case. The devices shown which used carbon nanotube films

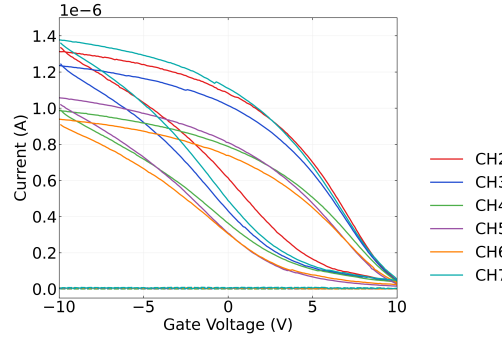
1. Characteristics of Pristine Carbon Nanotube & Graphene Field Effect Transistors



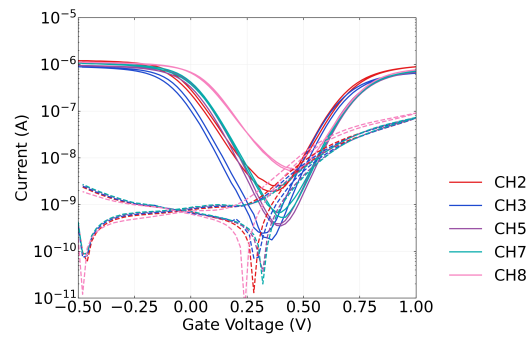
(a) Solvent-based deposition, back-gated



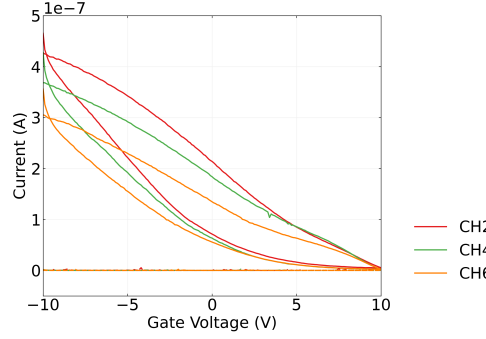
(b) Solvent-based deposition, liquid-gated



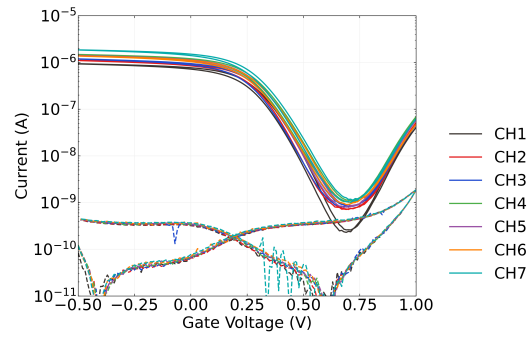
(c) Dropcast surfactant-based deposition, back-gated



(d) Dropcast surfactant-based deposition, liquid-gated



(e) Steam-assisted dropcast surfactant-based deposition, back-gated



(f) Steam-assisted dropcast surfactant-based deposition, liquid-gated

Figure 1.5.: Transfer characteristics of AZ® 1518 encapsulated field-effect transistors with carbon nanotube network channels deposited using various methods. 1XPBS was used as the buffer for the liquid-gated measurements here. The source-drain voltage used for all sweeps was $V_{ds} = 100\text{mV}$. A step size of 20 mV was used for the liquid-gated sweeps, while a step size of 100 mV was used for the backgated sweeps. Each pair of sweeps was taken from a separate device. Devices with a 100 nm SiO₂ layer were used for backgated measurements, and devices with a 300 nm SiO₂ layer were used for liquid gated measurements.

1.3. Electrical Characteristics of Pristine Devices

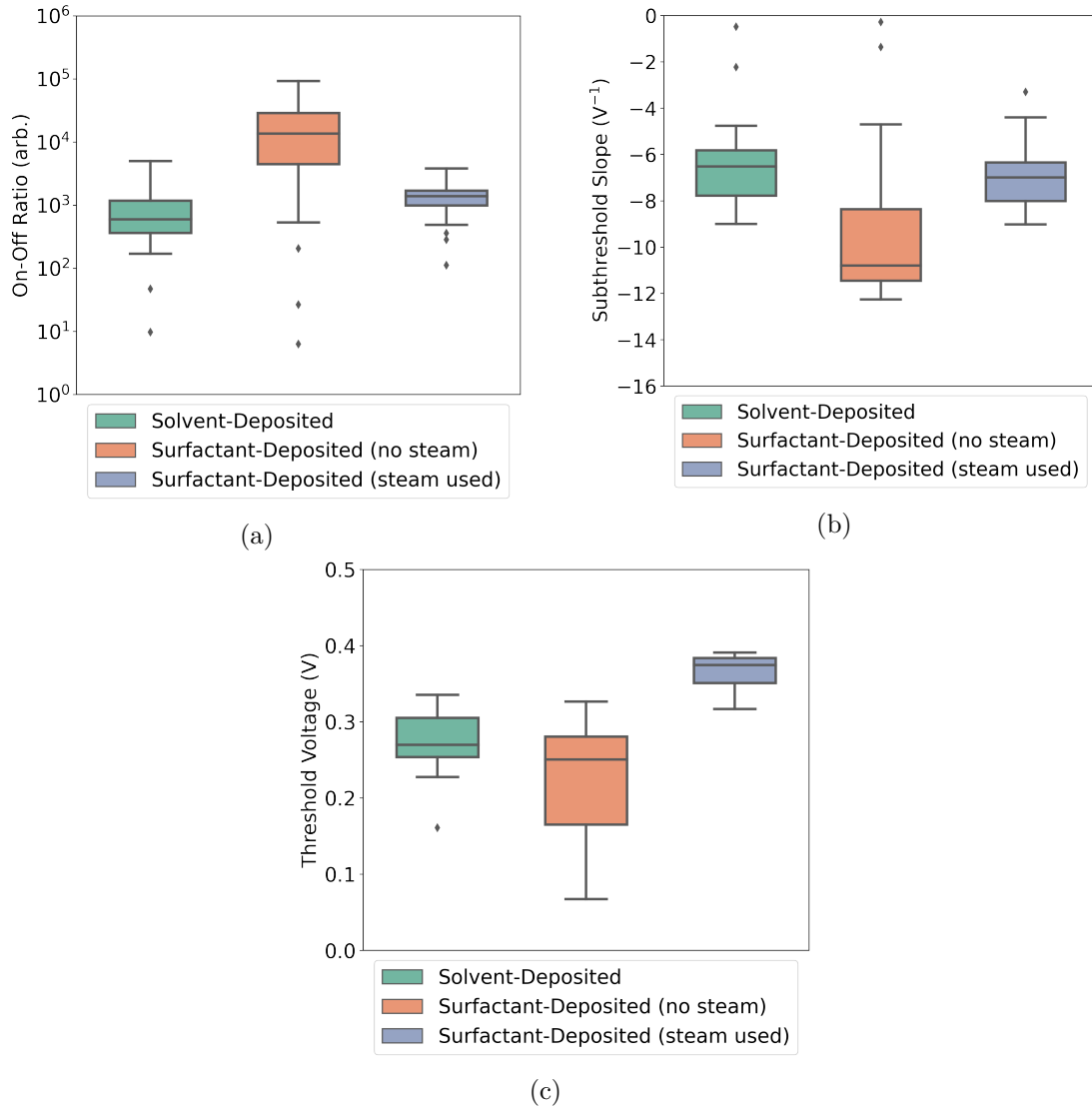


Figure 1.6.: These boxplots illustrate the statistical distribution of (a) the on-off ratio, (b) the subthreshold slope, and (c) the threshold voltage of AZ® 1518 encapsulated liquid-gated transistor channels corresponding to each type of carbon nanotube film deposition. For each deposition type, electrical characteristics were taken of 21 channels of at least three separate devices. The boxes indicate the 25th and 75th percentile of the distribution.

1. Characteristics of Pristine Carbon Nanotube & Graphene Field Effect Transistors

deposited in surfactant with steam present showed the least hysteresis, which is largely due to the relatively small diameter of the bundles in these films [30]. These devices also showed significantly less channel-to-channel variation in electrical characteristics more generally. A summary of key parameters of pristine liquid-gated devices is shown in Figure 1.6. The full dataset consists of three sets of 21 liquid-gated transfer characteristics of working channels, with each set corresponding to the use of a particular method of carbon nanotube network deposition in the device fabrication. Measurements from at least three devices are included in each set. Each entry in the summary corresponds to the average of the specific parameter in the forward and reverse sweep direction.

Channels from surfactant-deposited film devices usually showed a larger on-off ratio and subthreshold slope than those from solvent-deposited devices. When the transistor is gated in the subthreshold range, a larger on-off ratio and subthreshold slope results in a larger change in conductance in response to changes in the transfer characteristic curve. Therefore, a larger on-off ratio and subthreshold slope is desirable for improved sensor performance [25], [26], [31]. The larger on-off ratio for surfactant-deposited film devices is likely a result of the reduced bundling of nanotubes, as discussed in Section 1.2. Carbon nanotube pathways across the channel with a lower degree of bundling will have a lower number of component metallic tubes in the network, which increases the on-off ratio [2], [10], [32]. The effect of metallic nanotubes increasing the off current of a device channel is illustrated by channel 1 in Figure 1.5b. The larger subthreshold slope is likely due to increased mobility from a denser nanotube network in surfactant-deposited films [32], as seen in Figure 1.1.

When steam is used for surfactant deposition of films, the resulting devices showed highly consistent channel-to-channel electrical properties. As the carbon nanotube films on these devices are relatively dense, as seen in Figure 1.1, we know that the network is well above the percolation threshold. As many carbon nanotube pathways connect across the channel in parallel, small variations in the network morphology have less of an impact on the overall channel behaviour [2]. We also see from Table 1.2 that the range of bundle sizes is relatively low in the steam-deposited films used in these devices. The low range of bundle sizes means the semiconducting-metallic nanotube ratio is far more consistent for these devices, leading to more consistent electrical device characteristics. Being able to achieve consistent subthreshold regime behaviour between channels on the same device is a desirable attribute for reliable real-time multiplexed biosensing [25], [26], [31].

All channels characterised had a positive threshold voltage (V_{th}). The threshold voltage was largest and most consistent for steam-assisted surfactant-deposited films. The relatively high values of V_{th} which correspond to channel measurements from steam-assisted surfactant-deposited devices indicates increased *p*-doping of the network relative to networks deposited via alternative processes [2], [33], [34]. It is highly likely the dopant is present due to the steam deposition, and may be related to the large contamination peak for steam-deposited films seen in Figure 1.1 and [?@fig-remaining-histogram](#).

1.3. Electrical Characteristics of Pristine Devices

One possibility is that this dopant is residual surfactant, which can *p*-dope carbon nanotubes as well as enhancing *p*-doping from adsorbed oxygen and water [21], [35]. We have seen that steam prevents bundling of carbon nanotubes during deposition. This effect is likely due to persistence of the surfactant keeping nanotubes separate during this process. Presence of surfactant may also explain the lowered subthreshold slope and therefore mobility of the surfactant-deposited devices with steam relative to the surfactant-deposited devices without steam. The analysis by Kane *et al.* shows that the thermal annealing at 150°C used in this work to remove residual surfactant is likely inadequate for this purpose [21].

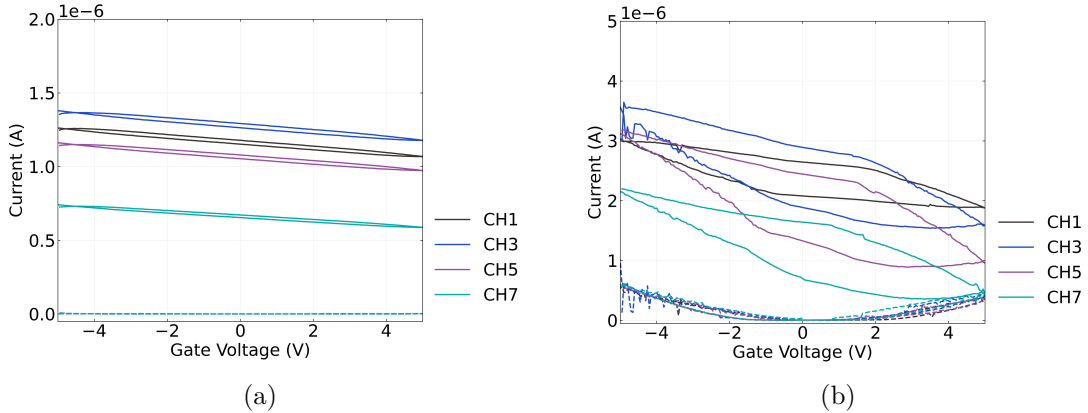


Figure 1.7.: Backgated transfer sweeps were taken of an single unencapsulated device with a 300 nm SiO₂ layer and steam assisted surfactant-deposited carbon nanotube network channels before and after being covered in 50 μ L 1XPBS electrolyte.

Figure 1.7 shows the behaviour of an unencapsulated backgated device with a 300 nm SiO₂ layer before and after being covered by 50 μ L of 1XPBS (phosphate buffered saline). The on-off ratio and hysteresis of the channels increase significantly. The presence of water increases hysteresis through introducing charge traps at the silicon dioxide surface around the carbon nanotubes and at the surface of the nanotubes themselves. The use of alternative transistor dielectrics and/or device functionalisation could potentially be used to reduce this hysteresis, as the time variation in threshold voltage due to hysteresis is unwanted for biosensing work [22], [24], [36], [37]. The electrical double layer formed by the electrolyte at the surface of the carbon nanotubes will also have contributed to the observed change in electrical properties, as it screens surface charge present on the surface around the nanotubes [38].

There is also a significant increase in current leakage to the backgate for larger applied voltages, despite the electrolyte having no visible physical contact with the silicon backgate or copper plane. This leakage current may simply be due to an increase in relative humidity around the device due to the presence of water [39].

1. Characteristics of Pristine Carbon Nanotube & Graphene Field Effect Transistors

1.3.2. Graphene Devices

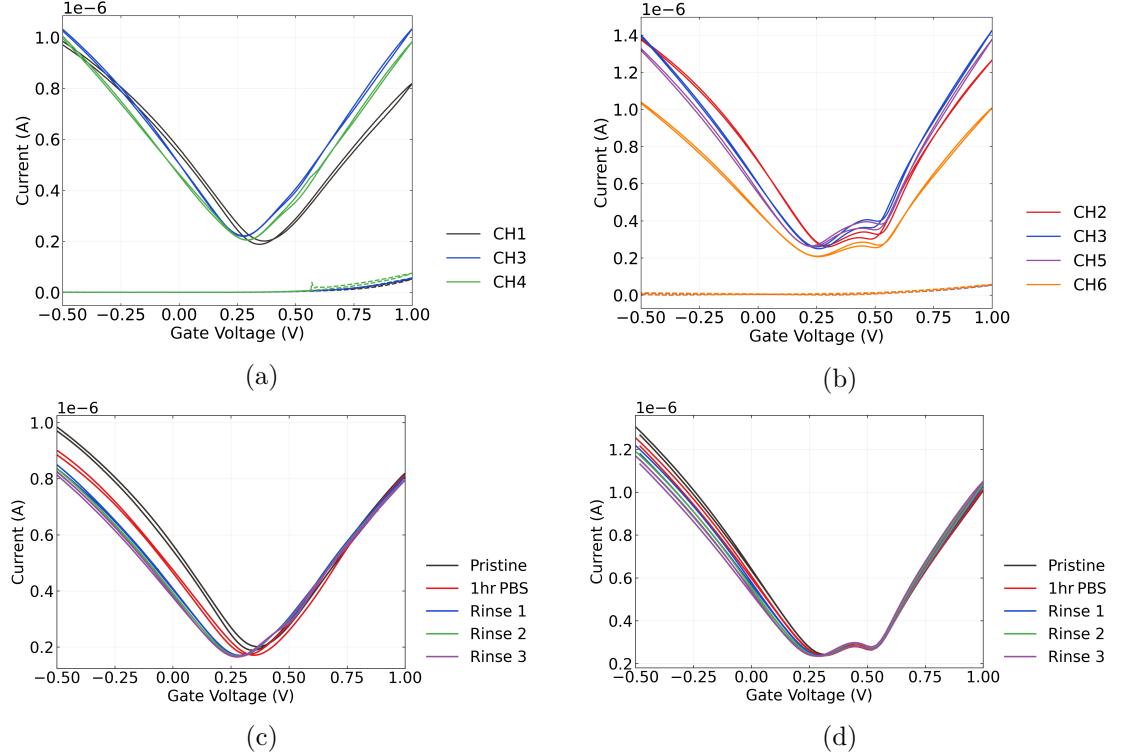


Figure 1.8.: These figures show liquid-gated transfer characteristics of channels from two AZ® 1518 encapsulated graphene devices. In (a) and (b), the characteristics of working device channels upon initial exposure to 1XPBS are displayed alongside gate current. The transfer characteristics of channel 1 in (a) and channel 5 in (b) after various degrees of exposure to 1XPBS are shown in (c) and (d) respectively.

Graphene devices were electrically characterised in the manner described in [?@sec-electrical-characterisation](#) and analysed using the Python code discussed in Section A.4.

Figure 1.8 shows the liquid-gated transfer characteristics of two graphene devices. These devices were fabricated prior to Jun 2021. Both devices exhibit the ambipolar characteristics typical of liquid-gated graphene devices [38], [40]–[42]. As with the carbon nanotube network devices, leakage current remained below $\sim 1 \times 10^{-7}$ V across both the forward and reverse sweep. Hysteresis between the forward and reverse sweep is caused by trapping of charge within and on the surface of the SiO₂ dielectric [43]. The major Dirac point for these devices is slightly to the right of $V_{\text{Dirac}} \approx 0$ V, which indicates *p*-doping of the channel. This slight *p*-doping is likely a result of a adsorption of oxygen and water from the air and residue resist from photolithography [42], [44], [45].

1.3. Electrical Characteristics of Pristine Devices

Table 1.3.: Average on-off ratio and major Dirac point voltage for AZ® 1518 encapsulated liquid-gated graphene transistor channels at various stages of exposure to 1XPBS. Electrical characteristics were taken of 6 channels total, three channels from each of two devices.

	1XPBS: Initial	1XPBS: After 1 hr	1XPBS: Rinse
On-Off Ratio (arb.)	5.1 ± 0.3	5.0 ± 0.7	5.0 ± 0.6
Dirac Point Voltage (V)	0.28 ± 0.04	0.31 ± 0.03	0.28 ± 0.02

Some devices exhibited a double-minima feature, indicating the presence of two Dirac points. This effect arises due to doping of graphene by the metal contacts. In shorter length channels, metal doping affects the entire channel length, leading to a consistent Fermi level and a single Dirac point. However, for longer channel lengths like ours, the doping effect from metal contact no longer reaches the entire channel, leading to a difference in Fermi level between the graphene in the channel and graphene under the metal contact. The difference in Fermi levels results in the presence of a second Dirac point [43], [46], [47]. The global minimum of the transfer characteristic can be referred to as the ‘major’ Dirac point.

Figure 1.8 also shows the effect of 1XPBS on the graphene channels. The channels were measured on exposure to 1XPBS, after exposure to 1XPBS for one hour, and after the device surface was rinsed and 1XPBS was replaced in the well one time, two times and three times successively. A slight negative shift of the major Dirac point was observed. This effect is possibly a result of gate bias stress, where successive transfer sweeps introduce charge traps to the graphene layer and alters the current level at a given gate voltage [48], [49]. Alternatively, Kireev *et al.* found that a series of liquid-gated sweeps also reduced the size of the second Dirac point, and suggested that it indicated the gate current was removing atmospheric contaminants from the graphene surface via current annealing [42]. This could be explained as the removal of contaminants causing improved contact between the metal and graphene surface, and thus increasing metal doping and consistency of the Fermi level across the channel. If the contaminants removed are *p*-dopants, then this effect could also explain the negative shift of the major Dirac point.

Table 1.3 shows the on-off ratio and major Dirac point voltage of the graphene devices. Apart from the previously-mentioned slight negative shift of the major Dirac point, these values were highly consistent before and after exposure to 1XPBS.

1.4. Real-Time Salt Concentration Sensing with Phosphate Buffered Saline

All devices analysed in this section were fabricated using steam-assisted, surfactant-deposited carbon nanotube network films.

1.4.1. Control Series and Baseline Drift

The total interval for the control series was 1800 s, with $20\mu\text{L}$ 1XPBS additions at 100 s, 200 s and 300 s, and $20\mu\text{L}$ subtractions at 400 s, 500 s and 600 s. Devices were left untouched over the next 1200 s to allow the current level to settle. Figure 1.9a shows the transfer sweep of a single channel of a steam-assisted surfactant-deposited device encapsulated with SU8, fabricated after Jun 2023. The threshold voltage of the channel is $V_{\text{th}} = 140$ mV, and the voltage corresponding to minimum current is $V_{\text{gap}} = 310$ mV. The variable symbol V_{gap} denotes the center of the transistor bandgap, has been labeled in this manner to be consistent with previous work [26].

Figure 1.9b shows two control series performed using the same channel on different days, with a different gate voltage used during each series. In both series, there is no clear stepwise response to any addition or subtraction of 1XPBS, as expected. We see that the current has a period of rapid decay followed by slower baseline drift, which has been observed previously for parallel arrangements of single carbon nanotubes in air or vacuum [49], [50]. This effect results from changes in the occupancy of charge traps in and around the substrate and carbon nanotubes. The magnitude of baseline drift is lower for our devices than for those characterised by Noyce *et al.*, which may be a result of numerous device and setup differences which affect the presence of charge traps. These differences include liquid-gating instead of back-gated, the use of a network of carbon nanotubes instead of single nanotubes, a different channel length, the use of a 300 nm instead of 90 nm SiO_2 layer, and the use of an asymmetric, liquid-gated transfer sweep over a shorter voltage range to characterise devices before each control series was measured [49].

As a first approximation to the longer time constant exponentials discussed by Noyce *et al.*, linear fits were performed on each control series from 1200 – 1800 s. The gradient of the $V_{\text{lg}} - V_{\text{gap}} = -200$ mV gated control series was $m_1 = -0.95 \pm 0.02$ pA/s, while the gradient of the $V_{\text{lg}} - V_{\text{gap}} = -150$ mV gated control series was $m_2 = -0.69 \pm 0.02$ pA/s. The equations for the two linear fits were proportional to each other, with $m_2 t + b_2 = (0.73 \pm 0.03) \times (m_1 t + b_1)$. This indicates a relationship between the voltage used to gate the devices and the degree of longer-term baseline drift. This effect is likely a consequence of gate bias stress, where gating introduces charge traps to the channel over time and reduces drain current. The more negative the applied bias, the larger the amplitude of the longer-term drift [48].

1.4. Real-Time Salt Concentration Sensing with Phosphate Buffered Saline

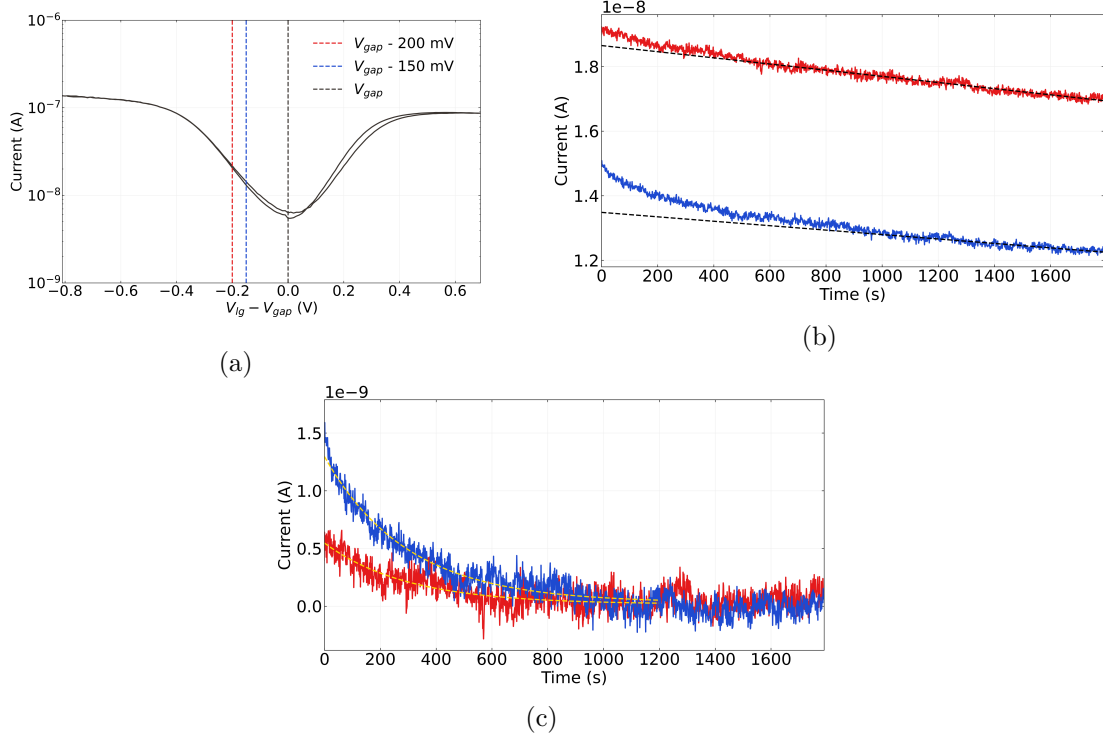


Figure 1.9.: The two gate voltages used during the control series in (b) are marked on the transfer characteristic in (a), where the transfer curve axis has been scaled so as to be centered around the minimum of the reverse sweep. The linear fits to the control series in (b) from 1200 s onwards had R squared values of 0.78 and 0.70 for the traces with gate voltage $V_{lg} - V_{gap} = -200$ mV and $V_{lg} - V_{gap} = -150$ mV respectively. The exponential fits in (c) from 0–1200 s had R squared values of 0.71 and 0.93 for the $V_{lg} - V_{gap} = -200$ mV and $V_{lg} - V_{gap} = -150$ mV traces respectively.

1. Characteristics of Pristine Carbon Nanotube & Graphene Field Effect Transistors

When the longer-term linear fits were subtracted from the raw data, the remaining dataset followed a exponential decay trend for both control series. Figure 1.9c shows exponential fits to the remaining curve from 0 – 1200 s. Both exponentials had a characteristic time constant of $\tau = 300 \pm 20$ s, indicating this rate of decay is independent of the gate voltage used to gate the transistor. They are therefore also proportional to each other, with $a_2 \exp(-t/\tau) = (2.39 \pm 0.05) \times a_1 \exp(-t/\tau)$. The $V_{\text{lg}} - V_{\text{gap}} = -200$ mV measurement was performed 3 days after the $V_{\text{lg}} - V_{\text{gap}} = -150$ mV measurement. It seems that the amplitude of the exponential term is history dependent and reduced with each subsequent control series. This behaviour is unlike that of the devices characterised by Noyce *et al.*, where the amplitude of the initial decay exponential remained the same after a initial reset gate sweep. It therefore appears that the sweep performed on these devices before measurement is insufficient to redistribute charges in trap states and reset the baseline drift, which could be a consequence of being liquid-gated instead of back-gated, being asymmetric or being over a shorter voltage range [49].

Figure 1.10a shows channel transfer characteristics from two different steam-assisted surfactant-deposited, AZ® 1518 encapsulated devices fabricated in different device batches. The central feature in the transfer characteristic in device 2 represents absolute-value measurements of ‘negative current’. These are unphysical measurements which come from equipment error and can be treated as zero current passing through the channel, and therefore V_{gap} is located in the center of this region. Device 1, with the channel characteristic curve shown in green, was fabricated in Mar 2023. Device 2, with the channel characteristic curve shown in purple, was fabricated after Jun 2023. Device 2 was flood exposed, rinsed with AZ® 326 developer and annealed at 150°C before measurement. When taking control series measurements, the devices were gated so that the current level for each control series would be as similar as possible, as illustrated by the dotted lines in Figure 1.10a.

As in Figure 1.9b, linear fits were performed on each control series from 1200 – 1800 s, shown in Figure 1.10b. The gradient of the control series corresponding to Device 1 was $m_1 = -8.2 \pm 0.1$ pA/s, while the gradient of the control series corresponding to Device 2 was $m_2 = -6.6 \pm 0.2$. Again, the equations for the two linear fits were proportional to each other, where $m_2 t + b_2 = (0.81 \pm 0.03) \times (m_1 t + b_1)$, despite being different channels from a different device batch. This result indicates that gate bias stress has the same effect on baseline drift on channels of different devices fabricated in the same manner.

As with the SU8 device, subtracting the linear fit resulted in a dataset which followed an exponential trend. Figure 1.10c shows exponential fits from 0 – 1200 s to the remaining curves from the AZ® 1518 devices. The time constants for these exponentials were dissimilar, with a time constant of $\tau = 141 \pm 3$ s for Device 1 and a time constant of $\tau = 408 \pm 11$ s for Device 2. The exponential amplitudes had opposite sign, with the first indicating an increase in net positive trapped charge and the latter indicating an increase in net negative trapped charge. It appears the difference in processing between the devices has changed the net charge of the traps initially present when measuring the control series.

1.4. Real-Time Salt Concentration Sensing with Phosphate Buffered Saline

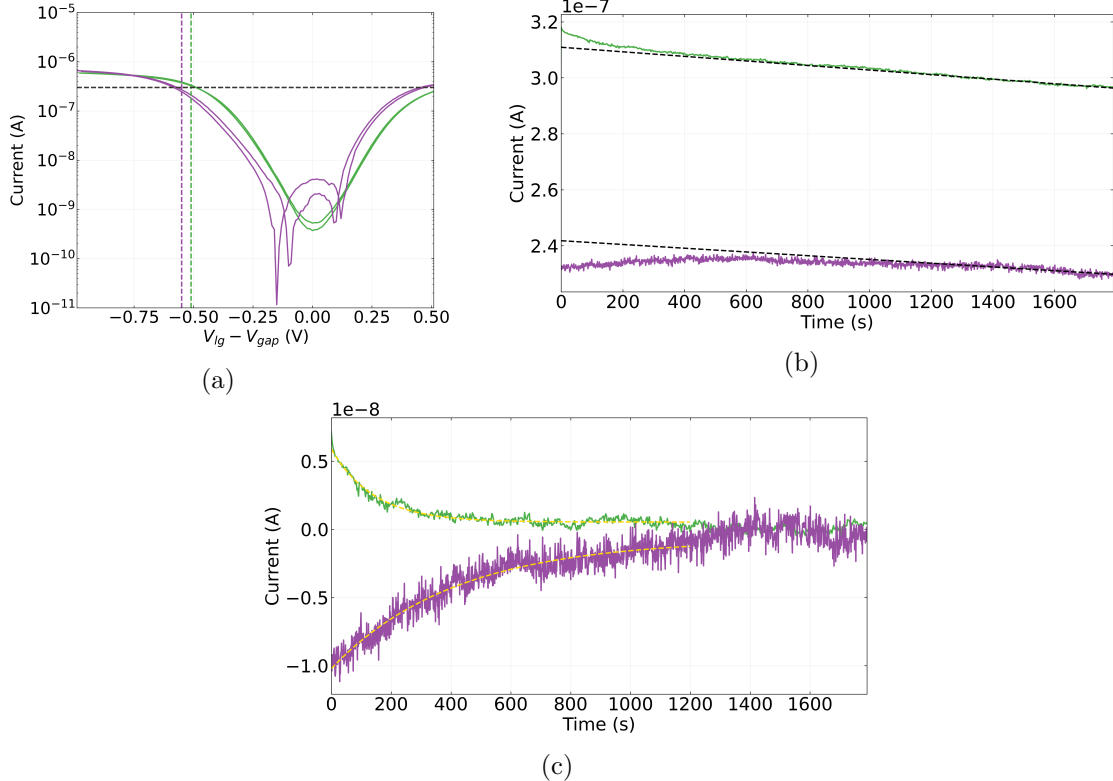


Figure 1.10.: The absolute-value transfer characteristics for the channels from Device 1 and Device 2 used in the control series in (b) are shown in (a), coloured green and purple respectively. The transfer curve axis has been scaled so as to be centered around the minimum of the reverse sweep, or in the case of Device 2, the centre point between the voltages where current drops to zero in the reverse sweep. The gate voltages used for each device during the control series in (b) are marked on the transfer characteristics in (a) in the same colour as their corresponding device. The linear fits to the control series in (b) from 1200 s onwards had R squared values of 0.96 and 0.67, and the exponential fits in (c) from 0 – 1200 s had R squared values of 0.94 and 0.92 for Devices 1 & 2 respectively.

1. Characteristics of Pristine Carbon Nanotube & Graphene Field Effect Transistors

Table 1.4.: This table shows the times at which 20 μL additions were made to the PDMS well, with 300 s between each addition. The concentration in the well after each addition and the change in concentration after each addition are also shown. The well contained 80 μL of 1X PBS at 1800 s.

	1X PBS Addition	DI Water Additions				
Time (s)	2100	2400	2700	3000	3300	3600
Final PBS volume (μL)	100	120	140	160	180	200
Final PBS concentration	1X	0.83X	0.71X	0.63X	0.56X	0.50X
Δ PBS concentration	0	-0.17X	-0.12X	-0.09X	-0.07X	-0.06X

From this analysis it appears that the baseline drift for the liquid-gated carbon nanotube devices can be accurately approximated as a combination of a exponential and linear term. The linear term appears to be consistent across channels of a particular device type, with the size of this term increasing with increasingly negative gate bias. The time constant of the exponential term appears to be intrinsic to the channel being measured.

1.4.2. Sensing Series

A salt concentration sensing series were performed from 1800 s onwards, directly after the control series. Salt concentration testing was done to confirm the fabricated devices were sensitive to small environmental changes in their pristine state, to check for spurious signals, and to ensure gate current leakage or other confounding factors were not contributing to sensing responses. The PDMS well contained 80 μL 1X PBS at 1800 s. During the series, successive additions of deionised water were made to reduce the concentration of PBS in the well. An initial 1X PBS addition was performed at 2100s, to confirm no changes occurred during the control series that would interfere with sensing. All additions to the well in the sensing series and resulting changes to the PBS concentration in the well are shown in Table 1.4.

Figure 1.11a shows a multiplexed salt concentration sensing series from the channels of a single AZ® 1518 encapsulated device, measured with the NI-PXIe. The gate voltage used was 0.0 V; this meant current measurements were well above the magnitude of the subthreshold device current. Gate current measurements did not exceed 1 nA for the SU8 encapsulated devices, and did not exceed 10 nA for the AZ® 1518 devices. At each of the deionised water addition times, the current traces for at least two out of six channels showed a sharp, transient increase in current followed by a return to an increased baseline. This baseline follows the downwards drift discussed in Section 1.4.1. It is well established that changing the salt concentration of the liquid gate has an electrostatic gating effect on the carbon nanotubes or graphene, and changes the transfer characteristics of the channel. This shift in transfer characteristic means we observe a realtime signal response to each addition [26], [38], [42].

1.4. Real-Time Salt Concentration Sensing with Phosphate Buffered Saline

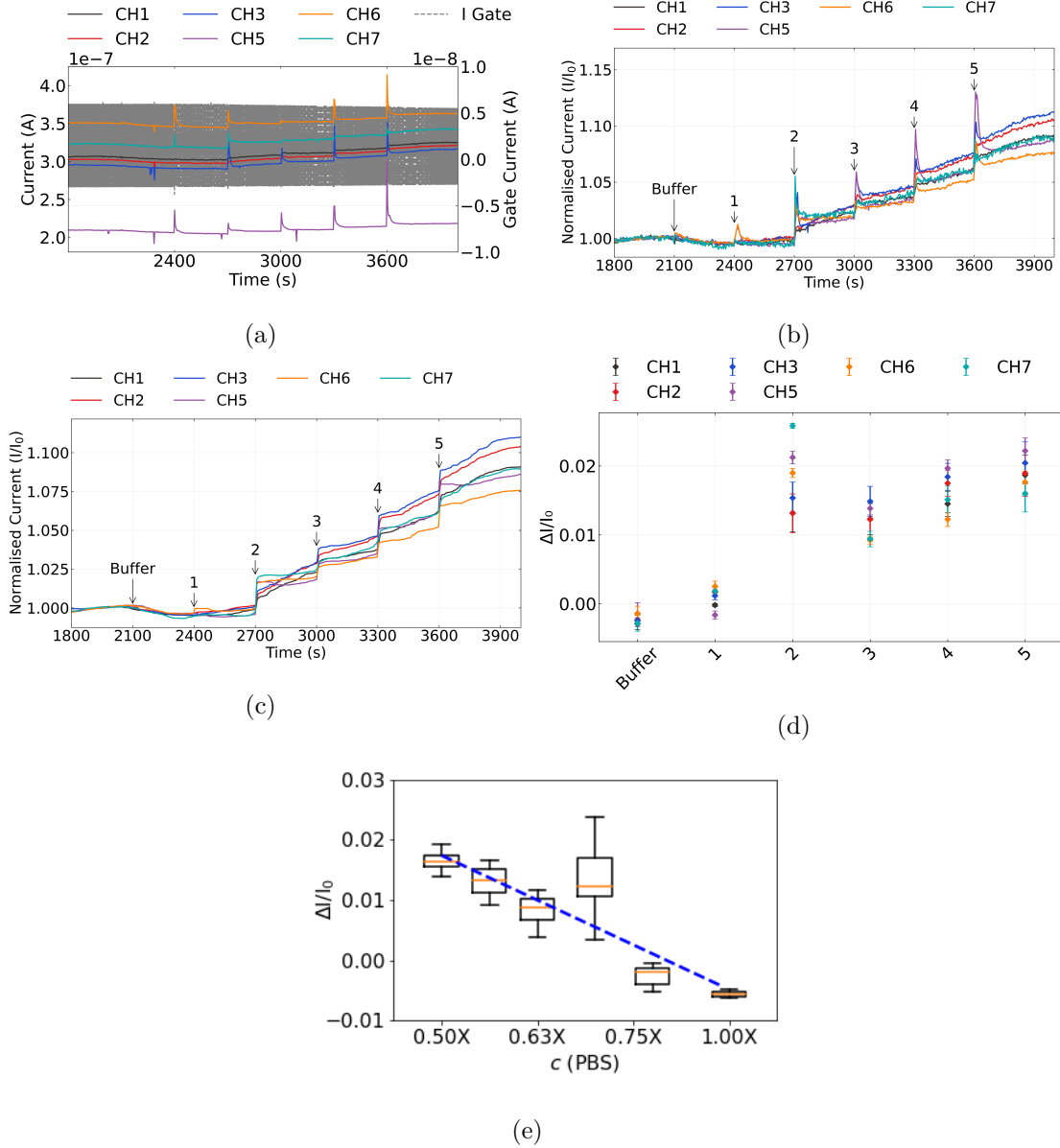


Figure 1.11.: Various visualisations of a multiplexed salt concentration sensing series taken from a single device. In (a), the raw current measurements for each channel are shown alongside gate current. The same measurements after despiking, removal of baseline drift and normalisation to initial current are shown in (b), (c) shows the data in (b) after being processed with a moving median filter, and (d) shows the signal changes in (c). The signal data in (d) is shown in box plot format in (e) alongside a fit to the median change in signal for each addition. The R squared value for the fit was 0.86.

1. Characteristics of Pristine Carbon Nanotube & Graphene Field Effect Transistors

Following the discussion in Section 1.4.1, we can subtract the linear term approximating baseline drift (mt) for each channel from the data in Figure 1.11a to account for the downward drift. The mean current level just before 1800 s then becomes roughly constant. We then normalise each channel relative to their initial mean current level I_0 . We also remove artifacts resulting from PXIe-2737 module lag, single datapoints which fall well below the current level of the immediately preceding and succeeding datapoints. This ‘despike’ process uses an interquartile range filter, as discussed in Section A.4. The resulting dataset is shown in Figure 1.11b. This figure shows that the signal-to-noise ratio remains roughly similar across all channels of the device. However, the behaviour of the initial transient increase with each addition is highly variable across channels and between additions for a single channel.

As measurement of the highly variable initial transient is not useful for robust sensing purposes, we can apply a moving median filter to the dataset, discussed further in Section A.4. The filtered data is shown in Figure 1.11c. Noise and initial transients are removed completely, while the clearly defined step to a new current baseline is retained. Using the realtime data in Figure 1.11c, a plot of signal against addition can be created using the method described in Section A.4, shown in Figure 1.11d. This presentation of the data allows us to see the increase at each step relative to I_0 .

Intriguingly, even though the largest change in PBS concentration occurred at the first deionised water addition (see Table 1.4), there was very little signal change across all channels, while a relatively large change occurred at the second addition. The logarithm of final salt concentration has previously been shown to be proportional to conductance change in the linear on-regime [38]. Figure 1.11e shows the signal change presented in terms of this logarithmic relationship. We see that the median values of the first two additions do not line up well with the overall logarithmic trend. Insufficient mixing in the tightly enclosed PDMS well environment for the first few additions may be responsible for this result. Subsequent additions may improve mixing in the well, leading to the change in concentration at the surface of the channel being more representative of the overall concentration in the well.

In Figure 1.11b and Figure 1.11c, we see that the drift behaviour of individual channels begin to significantly diverge from one another from roughly the second deionised water addition onwards. This deviation from the baseline drift subtracted from the raw data occurs either because the linear fit is only a first-order approximation which weakens with time, or because the additions themselves affect the drift behaviour. Displaying the data as discrete signal changes, as in Figure 1.11d, is one way of excluding these deviations (see Section A.4). An alternative way of presenting the signal changes, by normalising relative to both I_0 and the final current reading, is shown in Figure 1.12. This approach is useful for comparing unaccounted-for drift behaviour as well as the initial transient responses to additions between the channels of a multiplexed device.

Figure 1.12a demonstrates that the transient increases are consistently largest for channels in the center of the device, and smaller for those on the device edges (channels 1 & 2). This spatially-dependent behaviour may indicate responses are determined by

1.4. Real-Time Salt Concentration Sensing with Phosphate Buffered Saline

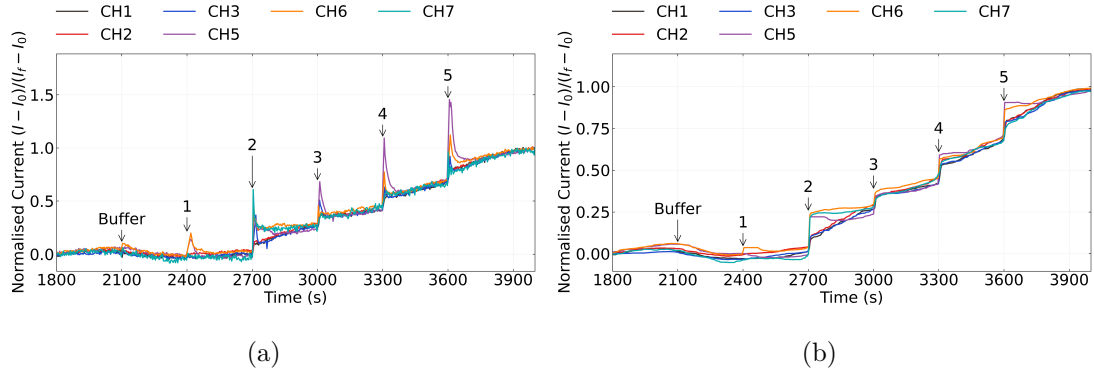


Figure 1.12.: If normalised so that the size of signal change is measured relative to the final instead of initial current, Figure 1.11b and Figure 1.11c can be shown as (e) and (f) respectively.

the location of placement of the water additions along the surface of the electrolyte in the well. From Figure 1.12b, where the transient responses are largely filtered out, we see clearly that the signal response relative to drift is highly consistent between channels. This result demonstrates that once unaccounted-for drift behaviour is removed, the signal size in response to each addition is highly consistent between channels. Slight deviations from the overall trend, such as for channels 5, 6 and 7 at deionised water addition 2, and for channels 5 and 6 at deionised water addition 5, are likely due to the large transient spikes at these channels not being completely filtered out by the median filter.

Signal-to-Noise Ratio

To compare signal-to-noise ratio between different gate currents and device configurations, the initial additions post-1800 s from the current traces in Figure 1.9 that were discussed earlier in Section 1.4.1 are shown in Figure 1.13. Previous work on the signal-to-noise ratio for liquid-gated, encapsulated carbon nanotube devices suggests that gating devices close to V_{gap} should give the largest signal-to-noise ratio for salt concentration additions [26]. However, as shown by Figure 1.9, this relationship was not consistently observed. This discrepancy could be a result of the use of a network of carbon nanotubes rather than a single nanotube; gating may have less of an impact on noise when a network morphology is used. Alternatively, it could be a result of a lack of mixing in our static well setup leading to inconsistent signal sizes with concentration change. Heller *et al.* used a flow cell during their signal-to-ratio work [26].

1. Characteristics of Pristine Carbon Nanotube & Graphene Field Effect Transistors

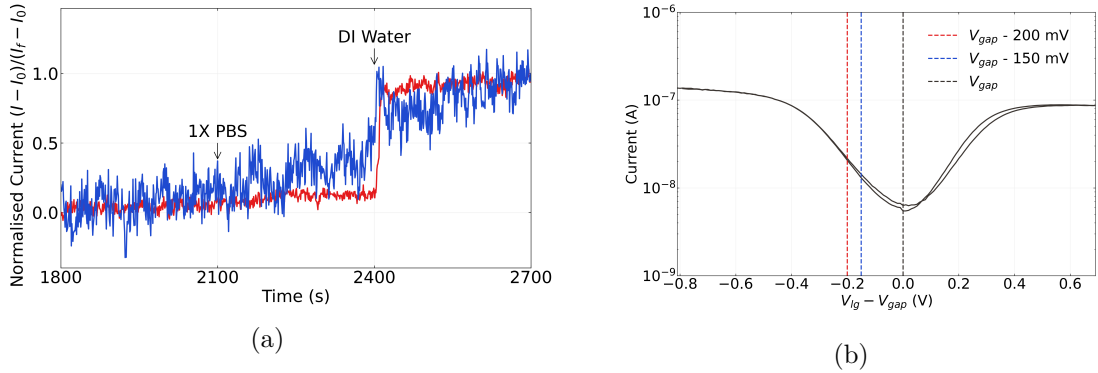


Figure 1.13.: The signal-to-noise ratio of the first deionised water addition for the traces seen in Figure 1.9 are shown in (a). For convenience, the transfer characteristics of the three channels in Figure 1.9, showing the two gate voltages used for measurements of a single SU8-encapsulated channel, are shown again in (b).

1.5. Conclusion

To ensure fabricated transistors were suitable for biosensing purposes, the morphology and electrical properties of the pristine carbon nanotube and graphene transistors were investigated.

The morphology of the carbon nanotube networks were found to have a significant impact on the electrical characteristics of the devices, which was determined through comparison of the height profile of the carbon nanotube network and the key electrical parameters of a range of carbon nanotube devices. When networks were highly bundled ($> 90\%$), there was a large range of carbon nanotube bundle diameters present in the network. This large variation in the size of conducting pathways resulted in a wide range of on-off ratios and threshold voltages for the liquid-gated devices created using these carbon nanotube films. In contrast, devices using films fabricated with a relatively low percentage of bundling ($< 75\%$) showed highly consistent on-off ratios and threshold voltages, along with low hysteresis, due to the relatively consistent bundle diameters and high density of these networks. These low-bundling networks were found to have a mean bundle distribution height of 3.2 ± 1.1 nm. When performing multiplexed sensing, consistent channel behaviour is highly desirable since comparing sensing behaviour between channels is more straightforward.

However, atomic force microscope images of low bundling networks also indicated that these networks have the most contamination present on the surface of the film relative to carbon nanotubes. This is possibly the cause of the increased threshold voltage of devices with films deposited with steam present relative to those using films fabricated without steam. The steam deposition may introduce *p*-dopants to the carbon nanotubes, which

1.5. Conclusion

could be due to surfactant left over from the deposition process. Since the presence of surfactant could negatively impact biosensing, techniques to remove contaminants should be explored in more detail. Thermal annealing of carbon nanotube films at high temperature is one approach that could be taken to resolve this issue, which is discussed further in ?@sec-future-work. The presence of electrolyte on the surface of a backgated transistor was also found to significantly adversely affect its electrical characteristics.

Constant voltage real-time measurements of the carbon nanotube devices had a characteristic drift that could be modelled using a exponential and linear term. The linear term of baseline drift appeared to be characteristic to the type of device measured, where the equation of the trendline for linear drift was proportionally related between channels fabricated in the same manner. An increase in device current level therefore meant an increase in the degree of linear drift. The time constant of the exponential term appeared to be characteristic to the particular channel used, with a time constant of $\tau = 300 \pm 20$ s for the SU8-encapsulated channel characterised, and time constants of $\tau = 141 \pm 3$ s and $\tau = 408 \pm 11$ s for the AZ® 1518 devices characterised.

Salt concentration sensing series indicated that the carbon nanotube transistor devices were highly sensitive to environmental changes and therefore suitable for sensing work. Successive additions of deionised water to the 1X PBS present in the well gave signal responses of up to 2.5 % above the control response. The signal response was found to be proportional to the logarithm of concentration, giving a fit to the median response sizes with an $R^2 = 0.86$. Deviations from this trend can possibly be explained by the enclosed sensing environment preventing sufficient mixing of electrolyte concentrations within the PDMS well. It was also seen that the relative signal size to baseline drift was highly consistent between channels. This is a promising result when it comes to ensuring consistent multiplexin, but it remains to be seen if this behaviour carries over to sensing with biofunctionalised devices.

Graphene devices were often found to possess a double-minima feature, which appears to be the result of a lack of doping from the metal contacts in the center of the device channels. These double Dirac points are unlikely to have an significant effect on the sensing behaviour of graphene devices. The graphene device characteristics were found to be consistent after 1 hour exposure to 1X PBS with minimal drift, with an on-off ratio of 5 and major Dirac point voltage of 0.3 V. There was some indications from the transfer characteristics that *p*-dopants were present on the graphene surface.

A. Python Code for Data Analysis

A.1. Code Repository

The code used for general analysis of field-effect transistor devices in this thesis was written with Python 3.8.8. Contributors to the code used include Erica Cassie, Erica Happe, Marissa Dierkes and Leo Browning. The code is located on GitHub and the research group OneDrive, and is available on request.

A.2. Atomic Force Microscope Histogram Analysis

The purpose of this code is to analyse atomic force microscope (AFM) images of carbon nanotube networks in .xyz format taken using an atomic force microscope and processed in Gwyddion (see [?@sec-afm-characterisation](#)). It was originally designed by Erica Happe in Matlab, and adapted by Marissa Dierkes and myself for use in Python. The code imports the .xyz data and sorts it into bins 0.15 nm in size for processing. To perform skew-normal distribution fits, both *scipy.optimize.curve_fit* and *scipy.stats.skewnorm* modules are used in this code.

A.3. Raman Spectroscopy Analysis

The purpose of this code is to analyse a series of Raman spectra taken at different points on a single film (see [?@sec-raman-characterisation](#)). Data is imported in a series of tab-delimited text files, with the low wavenumber spectrum ($100\text{ cm}^{-1} - 210\text{ cm}^{-1}$) and high wavenumber spectrum ($1250\text{ cm}^{-1} - 1735\text{ cm}^{-1}$) imported in separate datafiles for each scan location.

A.4. Field-Effect Transistor Analysis

The purpose of this code is to analyse electrical measurements taken of field-effect transistor (FET) devices. Electrical measurements were either taken from the Keysight 4156C Semiconductor Parameter Analyser, National Instruments NI-PXIe or Keysight B1500A Semiconductor Device Analyser as discussed in [?@sec-electrical-characterisation](#);

A. Python Code for Data Analysis

the code is able to analyse data taken from all three measurement setups. The main Python file in the code base consists of three related but independent modules: the first analyses and plots sensing data from the FET devices, the second analyses and plots transfer characteristics from channels across a device, and the third compares individual channel characteristics before and after a modification or after each of several modifications. The code base also features a separate config file and style sheet which govern the behaviour of the main code. The code base was designed collaboratively by myself and Erica Cassie over GitHub using the Sourcetree Git GUI.

The first of the three modules is for processing sensing datasets. This module imports sensing measurements in .csv format and analyses them, then outputs a plot of the raw data, alongside multiple plots which have been modified in various ways. It can also fit exponential and linear trendlines to regions of the sensing data, as well as find the signal change per analyte addition, and returns spreadsheets containing the results of these analyses. These spreadsheets include the standard deviation for all included parameters. Modified plots include normalised plots (type of normalisation can be set in config file), plots with fitted curves, plots with the linear baseline drift removed, plots of signal with analyte addition, “despiked” plots and “filtered” plots. It is possible to add annotations to any of these plots using the config file, and it is possible to produce a plot with a combination of these modifications.

The `scipy.optimize.curve_fit` module is used to fit linear and exponential curves to regions of interest of the sensing data. Initial parameters for the `scipy.optimize.curve_fit` module are chosen by approximating fitting parameters in a similar manner to the approach in Section A.2. For a linear fit $mt + b$, the parameters are simply set as $m = 1$ and $b = 0$. For an exponential fit $a \exp(-t/\tau) + c$, c is set as the final current measurement of the region of interest and a is set as the initial current measurement minus c . Then, τ is set as the time where current has dropped to $e^{-1}a + c$.

“Despiked” plots have had spurious datapoints removed through the use of an interquartile range rolling filter. The window size of the rolling filter used was 40 datapoints, and datapoints in each window with a z-score above ± 3 were removed from the plotted/processed data. “Filtered” plots had noise reduced using a moving median filter. The moving median filter is more effective at removing noise than a simple moving average, and has advantages over other filters (such as the Savitzky-Golay filter) when removing noise from data with sharp edges, as is the case for sensing data. Median filtering can also be used for baseline drift compensation, though this approach was not used in this thesis [51]. The moving median filter used had a window of 40 datapoints.

Plots of signal with analyte addition were constructed from current data after first removing baseline drift and applying a moving median filter. A simple difference calculation between the mean of the filtered current before an addition and the mean of the filtered current after the addition was performed at each addition. These differences were then normalised relative to the initial current. The signal with analyte addition give reasonably consistent results regardless of whether baseline drift was removed from the data,

A.4. Field-Effect Transistor Analysis

as shown in Figure A.1. We can therefore be confident that robust signal with analyte addition plots are robust even in the presence of significant drift.

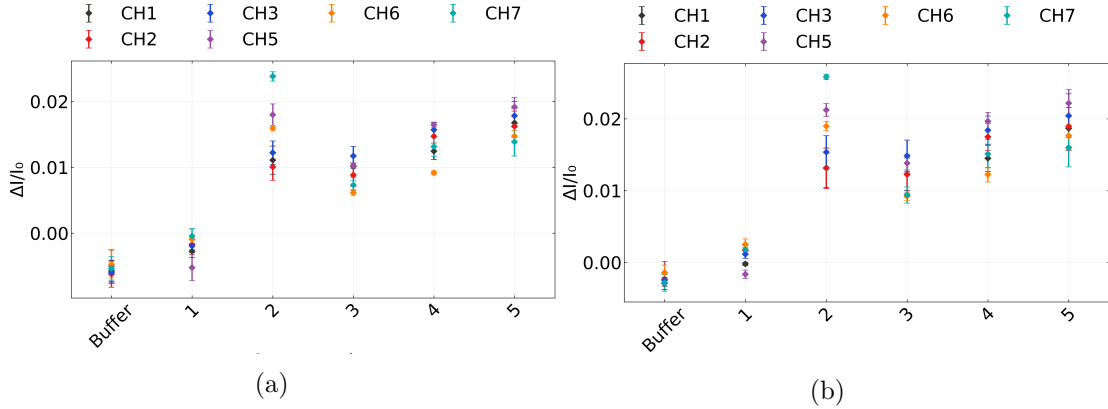


Figure A.1.: A comparison of signal with analyte addition plots taken from the same salt concentration sensing dataset (the same dataset as used in Figure 1.11). In (a), a simple difference calculation performed on filtered data was used, while in (b) the same calculation was performed on filtered data with the baseline drift removed, the method used in the body of the thesis.

The second module imports transfer measurements in .csv format and creates combined and individual plots of the eight channels on a single device. In combined plots, channels which are non-working, due to being shorted or non-conducting, are removed via setting a maximum and minimum possible on-current in the config file. Various parameters from the transfer characteristics are saved as a spreadsheet along with standard error. These parameters include on current, off current, subthreshold slope and threshold voltage for the carbon nanotube devices, and on current, off current and major Dirac point voltage for graphene devices. The device type being analysed can be set in the config file.

The third module imports several transfer measurements in .csv format and allows for comparison of the same channel before and after some modification. It also calculates the shift in either threshold voltage or major Dirac voltage of the device.

Bibliography

- [1] H. Y. Zheng and N. O.V. Plank. “Facile fabrication of carbon nanotube network thin film transistors for device platforms”. In: *International Journal of Nanotechnology* 14.1-6 (2017), pp. 505–518. ISSN: 14757435. DOI: 10.1504/IJNT.2017.082473.
- [2] Thanihaichelvan Murugathas, Leo A. Browning, Marissa P. Dierkes, et al. “Data on liquid gated CNT network FETs on flexible substrates”. In: *Data in Brief* 21 (Dec. 2018), pp. 276–283. ISSN: 2352-3409. DOI: 10.1016/J.DIB.2018.09.093.
- [3] Thanihaichelvan Murugathas, Leo A. Browning, Marissa P. Dierkes, et al. “Metallic-semiconducting junctions create sensing hot-spots in carbon nanotube FET aptasensors near percolation”. In: *Biosensors and Bioelectronics* 130 (Apr. 2019), pp. 408–413. ISSN: 0956-5663. DOI: 10.1016/J.BIOS.2018.09.021.
- [4] Hong Phan T. Nguyen, Thanihaichelvan Murugathas, and Natalie O.V. Plank. “Comparison of Duplex and Quadruplex Folding Structure Adenosine Aptamers for Carbon Nanotube Field Effect Transistor Aptasensors”. In: *Nanomaterials (Basel, Switzerland)* 11.9 (Sept. 2021). ISSN: 2079-4991. DOI: 10.3390/NANO11092280. URL: <https://pubmed.ncbi.nlm.nih.gov/34578596/>.
- [5] Wim Wenseleers, Igor L. Vlasov, Etienne Goovaerts, et al. “Efficient Isolation and Solubilization of Pristine Single-Walled Nanotubes in Bile Salt Micelles”. In: *Advanced Functional Materials* 14.11 (Nov. 2004), pp. 1105–1112. ISSN: 1616-3028. DOI: 10.1002/ADFM.200400130. URL: <https://onlinelibrary.wiley.com/doi/full/10.1002/adfm.200400130%20https://onlinelibrary.wiley.com/doi/abs/10.1002/adfm.200400130%20https://onlinelibrary.wiley.com/doi/10.1002/adfm.200400130>.
- [6] Gildas Gavrel, Bruno Jousselme, Arianna Filoromo, et al. “Supramolecular Chemistry of Carbon Nanotubes”. In: (2013), pp. 95–126. DOI: 10.1007/128_2013_450.
- [7] Greg T. Hermanson. “Buckyballs, Fullerenes, and Carbon Nanotubes”. In: *Bioconjugate Techniques* (Jan. 2013), pp. 741–755. DOI: 10.1016/B978-0-12-382239-0.00016-9.
- [8] Maki Shimizu, Shunjiro Fujii, Takeshi Tanaka, et al. “Effects of surfactants on the electronic transport properties of thin-film transistors of single-wall carbon nanotubes”. In: *Journal of Physical Chemistry C* 117.22 (June 2013), pp. 11744–11749. ISSN: 19327455. DOI: 10.1021/JP3113254/SUPPL_FILE/JP3113254_SI_001.PDF. URL: <https://pubs.acs.org/doi/full/10.1021/jp3113254>.

Bibliography

- [9] Antonello Di Crescenzo, Valeria Ettorre, and Antonella Fontana. “Non-covalent and reversible functionalization of carbon nanotubes”. In: *Beilstein Journal of Nanotechnology* 5.1 (2014), p. 1675. ISSN: 21904286. DOI: 10.3762/BJNANO.5.178. URL: [/pmc/articles/PMC4222398/](https://pmc/articles/PMC4222398/)?report=abstract%20https://www.ncbi.nlm.nih.gov/pmc/articles/PMC4222398/.
- [10] Melburne C. LeMieux, Mark Roberts, Soumendra Barman, et al. “Self-sorted, aligned nanotube networks for thin-film transistors”. In: *Science* 321.5885 (July 2008), pp. 101–104. ISSN: 00368075. DOI: 10.1126/SCIENCE.1156588. URL: <https://www.science.org>.
- [11] Chang Liu and Hui Ming Cheng. “Carbon nanotubes: controlled growth and application”. In: *Materials Today* 16.1-2 (Jan. 2013), pp. 19–28. ISSN: 1369-7021. DOI: 10.1016/J.MATTOD.2013.01.019.
- [12] Dusan Vobornik, Maohui Chen, Shan Zou, et al. “Measuring the Diameter of Single-Wall Carbon Nanotubes Using AFM”. In: *Nanomaterials* 13.3 (Feb. 2023), p. 477. ISSN: 20794991. DOI: 10.3390/NANO13030477/S1. URL: <https://www.mdpi.com/2079-4991/13/3/477>.
- [13] A. Azzalini and A. Capitanio. “Statistical applications of the multivariate skew normal distribution”. In: *Journal of the Royal Statistical Society Series B* 61.3 (1999), pp. 579–602. ISSN: 13697412. DOI: 10.1111/1467-9868.00194. arXiv: 0911.2093. URL: <https://ideas.repec.org/a/bla/jorss/v61y1999i3p579-602.html>%20https://ideas.repec.org//a/bla/jorss/v61y1999i3p579-602.html.
- [14] Matěj Velický, Adam J Cooper, Peter S Toth, et al. “Mechanical stability of substrate-bound graphene in contact with aqueous solutions”. In: *2D Materials* 2.2 (May 2015), p. 024011. ISSN: 2053-1583. DOI: 10.1088/2053-1583/2/2/024011. URL: [https://iopscience.iop.org/article/10.1088/2053-1583/2/2/024011%20https://iopscience.iop.org/article/10.1088/2053-1583/2/2/024011/meta](https://iopscience.iop.org/article/10.1088/2053-1583/2/2/024011).
- [15] R. L. Graham, B. D. Lubachevsky, K. J. Nurmela, et al. “Dense packings of congruent circles in a circle”. In: *Discrete Mathematics* 181.1-3 (Feb. 1998), pp. 139–154. ISSN: 0012-365X. DOI: 10.1016/S0012-365X(97)00050-2.
- [16] Eckard Specht. *The best known packings of equal circles in a circle*. URL: <http://hydra.nat.uni-magdeburg.de/packing/cci/cci.html> (visited on 2023-09-11).
- [17] Robert D. Deegan, Olgica Bakajin, Todd F. Dupont, et al. “Capillary flow as the cause of ring stains from dried liquid drops”. In: *Nature* 1997 389:6653 389.6653 (1997), pp. 827–829. ISSN: 1476-4687. DOI: 10.1038/39827. URL: <https://www.nature.com/articles/39827>.
- [18] R. T. van Gaalen, C. Diddens, H. M.A. Wijshoff, et al. “Marangoni circulation in evaporating droplets in the presence of soluble surfactants”. In: *Journal of Colloid and Interface Science* 584 (Feb. 2021), pp. 622–633. ISSN: 0021-9797. DOI: 10.1016/J.JCIS.2020.10.057.

- [19] Mindy D. Bishop, Gage Hills, Tathagata Srimani, et al. “Fabrication of carbon nanotube field-effect transistors in commercial silicon manufacturing facilities”. In: *Nature Electronics* 2020 3:8 3.8 (June 2020), pp. 492–501. ISSN: 2520-1131. DOI: 10.1038/s41928-020-0419-7. URL: <https://www.nature.com/articles/s41928-020-0419-7>.
- [20] Yulia V Marchenko and Marc G Genton. “A suite of commands for fitting the skew-normal and skew-t models”. In: *The Stata Journal* 10.4 (2010), pp. 507–539.
- [21] Alexander A. Kane, Alexandra C. Ford, April Nissen, et al. “Etching of surfactant from solution-processed, type-separated carbon nanotubes and impact on device behavior”. In: *ACS Nano* 8.3 (Mar. 2014), pp. 2477–2485. ISSN: 1936086X. DOI: 10.1021/NN406065T/SUPPL_FILE/NN406065T_SI_001.PDF. URL: <https://pubs.acs.org/doi/full/10.1021/nn406065t>.
- [22] Joon Sung Lee, Sunmin Ryu, Kwonjae Yoo, et al. “Origin of gate hysteresis in carbon nanotube field-effect transistors”. In: *Journal of Physical Chemistry C* 111.34 (Aug. 2007), pp. 12504–12507. ISSN: 19327447. DOI: 10.1021/JP074692Q/ASSET/IMAGES/LARGE/JP074692QF00003.JPG. URL: <https://pubs.acs.org/doi/full/10.1021/jp074692q>.
- [23] Sang Won Lee, Si Young Lee, Seong Chu Lim, et al. “Positive gate bias stress instability of carbon nanotube thin film transistors”. In: *Applied Physics Letters* 101.5 (July 2012). ISSN: 00036951. DOI: 10.1063/1.4740084/111432. URL: [/aip/apl/article/101/5/053504/111432/Positive-gate-bias-stress-instability-of-carbon](https://aip.org/apl/article/101/5/053504/111432/Positive-gate-bias-stress-instability-of-carbon).
- [24] Tae Jun Ha, Daisuke Kiriya, Kevin Chen, et al. “Highly stable hysteresis-free carbon nanotube thin-film transistors by fluorocarbon polymer encapsulation”. In: *ACS Applied Materials and Interfaces* 6.11 (June 2014), pp. 8441–8446. ISSN: 19448252. DOI: 10.1021/AM5013326/ASSET/IMAGES/LARGE/AM-2014-013326_0007.JPG. URL: <https://pubs.acs.org/doi/full/10.1021/am5013326>.
- [25] Douglas R. Kauffman and Alexander Star. “Electronically monitoring biological interactions with carbon nanotube field-effect transistors”. In: *Chemical Society Reviews* 37.6 (May 2008), pp. 1197–1206. ISSN: 1460-4744. DOI: 10.1039/B709567H. URL: <https://pubs.rsc.org/en/content/articlehtml/2008/cs/b709567h%20https://pubs.rsc.org/en/content/articlelanding/2008/cs/b709567h>.
- [26] Iddo Heller, Jaan Männik, Serge G. Lemay, et al. “Optimizing the signal-to-noise ratio for biosensing with carbon nanotube transistors”. In: *Nano Letters* 9.1 (Jan. 2009), pp. 377–382. ISSN: 15306984. DOI: 10.1021/NL8031636/SUPPL_FILE/NL8031636_SI_001.PDF. URL: <https://pubs.acs.org/doi/full/10.1021/nl8031636>.
- [27] Woo Jong Yu, Un Jeong Kim, Bo Ram Kang, et al. “Adaptive Logic Circuits with Doping-Free Ambipolar Carbon Nanotube Transistors”. In: *NANO LETTERS* 9.4 (2009), pp. 1401–1405. DOI: 10.1021/nl803066v. URL: <https://pubs.acs.org/sharingguidelines>.

Bibliography

- [28] Vladimir Derenskyi, Widiantha Gomulya, Jorge Mario Salazar Rios, et al. “Carbon Nanotube Network Ambipolar Field-Effect Transistors with 108 On/Off Ratio”. In: *Advanced Materials* 26.34 (Sept. 2014), pp. 5969–5975. ISSN: 15214095. DOI: 10.1002/ADMA.201401395.
- [29] Faris M. Albarghouthi, Nicholas X. Williams, James L. Doherty, et al. “Passivation Strategies for Enhancing Solution-Gated Carbon Nanotube Field-Effect Transistor Biosensing Performance and Stability in Ionic Solutions”. In: *ACS Applied Nano Materials* 5.10 (Oct. 2022), pp. 15865–15874. ISSN: 25740970. DOI: 10.1021/ACSANM.2C04098/SUPPL_FILE/AN2C04098_SI_001.PDF. URL: <https://doi.org/10.1021/acsanm.2c04098>.
- [30] Eric Pop, Sumit Dutta, David Estrada, et al. “Avalanche, Joule breakdown and hysteresis in carbon nanotube transistors”. In: *IEEE International Reliability Physics Symposium Proceedings* (2009), pp. 405–408. ISSN: 15417026. DOI: 10.1109/IRPS.2009.5173287.
- [31] Xuan P A Gao, Gengfeng Zheng, and Charles M Lieber. “Subthreshold Regime has the Optimal Sensitivity for Nanowire FET Biosensors”. In: (2010). DOI: 10.1021/nl9034219. URL: <https://pubs.acs.org/sharingguidelines>.
- [32] Nima Rouhi, Dheeraj Jain, Katayoun Zand, et al. “Fundamental limits on the mobility of nanotube-based semiconducting inks”. In: *Advanced Materials* 23.1 (Jan. 2011), pp. 94–99. ISSN: 09359648. DOI: 10.1002/ADMA.201003281.
- [33] Donghun Kang, Noejung Park, Ju Hye Ko, et al. “Oxygen-induced p-type doping of a long individual single-walled carbon nanotube”. In: *Nanotechnology* 16.8 (May 2005), p. 1048. ISSN: 0957-4484. DOI: 10.1088/0957-4484/16/8/008. URL: <https://iopscience.iop.org/article/10.1088/0957-4484/16/8/008%20https://iopscience.iop.org/article/10.1088/0957-4484/16/8/008/meta>.
- [34] Iddo Heller, Anne M. Janssens, Jaan Männik, et al. “Identifying the mechanism of biosensing with carbon nanotube transistors”. In: *Nano Letters* 8.2 (Feb. 2008), pp. 591–595. ISSN: 15306984. DOI: 10.1021/NL072996I/SUPPL_FILE/NL072996ISI20071116_124235.PDF. URL: <https://pubs.acs.org/doi/full/10.1021/nl072996i>.
- [35] Yoshiyuki Nonoguchi, Atsushi Tani, Tomoko Murayama, et al. “Surfactant-driven Amphoteric Doping of Carbon Nanotubes”. In: *Chemistry - An Asian Journal* 13.24 (Dec. 2018), pp. 3942–3946. ISSN: 1861471X. DOI: 10.1002/ASIA.201801490.
- [36] Woong Kim, Ali Javey, Ophir Vermesh, et al. “Hysteresis Caused by Water Molecules in Carbon Nanotube Field-Effect Transistors”. In: *NANO LETTERS* 3.2 (2003), pp. 193–198. DOI: 10.1021/nl0259232.
- [37] Aaron D. Franklin, George S. Tulevski, Shu Jen Han, et al. “Variability in carbon nanotube transistors: Improving device-to-device consistency”. In: *ACS Nano* 6.2 (Feb. 2012), pp. 1109–1115. ISSN: 19360851. DOI: 10.1021/NN203516Z/SUPPL_FILE/NN203516Z_SI_001.PDF. URL: <https://pubs.acs.org/doi/full/10.1021/nn203516z>.

- [38] Iddo Heller, Sohail Chatoor, Jaan Männik, et al. "Influence of electrolyte composition on liquid-gated carbon nanotube and graphene transistors". In: *Journal of the American Chemical Society* 132.48 (Dec. 2010), pp. 17149–17156. ISSN: 00027863. DOI: 10.1021/JA104850N/SUPPL_FILE/JA104850N_SI_001.PDF. URL: <https://pubs.acs.org/doi/full/10.1021/ja104850n>.
- [39] Helene Conseil, Morten S. Jellesen, and Rajan Ambat. "Experimental study of water absorption of electronic components and internal local temperature and humidity into electronic enclosure". In: *Proceedings of the 16th Electronics Packaging Technology Conference, EPTC 2014* (Jan. 2014), pp. 355–359. DOI: 10.1109/EPTC.2014.7028356.
- [40] I. Heller, S. Chatoor, J. Männik, et al. "Comparing the weak and strong gate-coupling regimes for nanotube and graphene transistors". In: *physica status solidi (RRL) – Rapid Research Letters* 3.6 (Sept. 2009), pp. 190–192. ISSN: 1862-6270. DOI: 10.1002/PSSR.200903157. URL: <https://onlinelibrary.wiley.com/doi/full/10.1002/pssr.200903157%20https://onlinelibrary.wiley.com/doi/abs/10.1002/pssr.200903157%20https://onlinelibrary.wiley.com/doi/10.1002/pssr.200903157>.
- [41] Fengnian Xia, Damon B. Farmer, Yu Ming Lin, et al. "Graphene field-effect transistors with high on/off current ratio and large transport band gap at room temperature". In: *Nano Letters* 10.2 (Feb. 2010), pp. 715–718. ISSN: 15306984. DOI: 10.1021/NL9039636/ASSET/IMAGES/LARGE/NL-2009-039636_0003.JPG. URL: <https://pubs.acs.org/doi/full/10.1021/nl9039636>.
- [42] Dmitry Kiriev, Max Brambach, Silke Seyock, et al. "Graphene transistors for interfacing with cells: towards a deeper understanding of liquid gating and sensitivity". In: *Scientific Reports* 2017 7:1 7.1 (July 2017), pp. 1–12. ISSN: 2045-2322. DOI: 10.1038/s41598-017-06906-5. URL: <https://www.nature.com/articles/s41598-017-06906-5>.
- [43] Antonio Di Bartolomeo, Filippo Giubileo, Salvatore Santandrea, et al. "Charge transfer and partial pinning at the contacts as the origin of a double dip in the transfer characteristics of graphene-based field-effect transistors". In: *Nanotechnology* 22.27 (May 2011), p. 275702. ISSN: 0957-4484. DOI: 10.1088/0957-4484/22/27/275702. URL: <https://iopscience.iop.org/article/10.1088/0957-4484/22/27/275702%20https://iopscience.iop.org/article/10.1088/0957-4484/22/27/275702/meta>.
- [44] Zengguang Cheng, Qiaoyu Zhou, Chenxuan Wang, et al. "Toward intrinsic graphene surfaces: A systematic study on thermal annealing and wet-chemical treatment of SiO₂-supported graphene devices". In: *Nano Letters* 11.2 (Feb. 2011), pp. 767–771. ISSN: 15306984. DOI: 10.1021/NL103977D/SUPPL_FILE/NL103977D_SI_001.PDF. URL: <https://pubs.acs.org/doi/full/10.1021/nl103977d>.

Bibliography

- [45] Dong Wook Shin, Hyun Myoung Lee, Seong Man Yu, et al. “A facile route to recover intrinsic graphene over large scale”. In: *ACS Nano* 6.9 (Sept. 2012), pp. 7781–7788. ISSN: 19360851. DOI: 10.1021/NN3017603/SUPPL_FILE/NN3017603_SI_001.PDF. URL: <https://pubs.acs.org/doi/full/10.1021/nn3017603>.
- [46] Tingting Feng, Dan Xie, Jianlong Xu, et al. “Back-gate graphene field-effect transistors with double conductance minima”. In: *Carbon* 79.1 (Nov. 2014), pp. 363–368. ISSN: 0008-6223. DOI: 10.1016/J.CARBON.2014.07.078.
- [47] Song ang Peng, Zhi Jin, Dayong Zhang, et al. “How Do Contact and Channel Contribute to the Dirac Points in Graphene Field-Effect Transistors?” In: *Advanced Electronic Materials* 4.8 (Aug. 2018), p. 1800158. ISSN: 2199-160X. DOI: 10.1002/AELM.201800158. URL: <https://onlinelibrary.wiley.com/doi/full/10.1002/aelm.201800158%20https://onlinelibrary.wiley.com/doi/abs/10.1002/aelm.201800158%20https://onlinelibrary.wiley.com/doi/10.1002/aelm.201800158>.
- [48] Y. Bargaoui, M. Troudi, P. Bondavalli, et al. “Gate bias stress effect in single-walled carbon nanotubes field-effect-transistors”. In: *Diamond and Related Materials* 84 (Apr. 2018), pp. 62–65. ISSN: 0925-9635. DOI: 10.1016/J.DIAMOND.2018.03.011.
- [49] Steven G. Noyce, James L. Doherty, Zhihui Cheng, et al. “Electronic Stability of Carbon Nanotube Transistors under Long-Term Bias Stress”. In: *Nano Letters* 19.3 (Mar. 2019), pp. 1460–1466. ISSN: 15306992. DOI: 10.1021/ACS.NANOLETT.8B03986/ASSET/IMAGES/LARGE/NL-2018-03986G_0005.JPG. URL: <https://pubs.acs.org/doi/full/10.1021/acs.nanolett.8b03986>.
- [50] H. Lin and S. Tiwari. “Localized charge trapping due to adsorption in nanotube field-effect transistor and its field-mediated transport”. In: *Applied Physics Letters* 89.7 (Aug. 2006), p. 73507. ISSN: 00036951. DOI: 10.1063/1.2337104/332595. URL: [/aip/apl/article/89/7/073507/332595/Localized-charge-trapping-due-to-adsorption-in](https://aip.org/article/89/7/073507/332595/Localized-charge-trapping-due-to-adsorption-in).
- [51] David C. Stone. “Application of median filtering to noisy data”. In: 73.10 (Oct. 2011), pp. 1573–1581. ISSN: 0008-4042. DOI: 10.1139/V95-195. URL: <https://cdnsciencepub.com/doi/10.1139/v95-195>.